Title
Nanoparticle-Based Activatable Probes for Bioimaging

Journal
Advanced Biology, 5(1)

ISSN
2701-0198

Authors
Ma, Tiancong
Xia, Tian

Publication Date
2021

DOI
10.1002/adbi.202000193

Peer reviewed

HHS Public Access

Author manuscript

Adv Biol (Weinh). Author manuscript; available in PMC 2022 January 04.

Published in final edited form as:

Adv Biol (Weinh). 2021 January ; 5(1): e2000193. doi:10.1002/adbi.202000193.

Nanoparticle-based activatable probes for bioimaging

Tiancong Ma[1,2], **Tian Xia**[1,*]

[1]Division of Nanomedicine, Department of Medicine, David Geffen School of Medicine, University of California, Los Angeles, California 90095-1772, USA

[2]Department of Environmental Health Sciences, Jonathan and Karin Fielding School of Public Health, University of California, Los Angeles, California 90095-1772, USA

Abstract

Molecular imaging can provide functional and molecular information at the cellular or subcellular level *in vivo* in a non-invasive manner. Activatable nanoprobes that can react to the surrounding physiological environment or biomarkers are appealing agents to improve the efficacy, specificity, and sensitivity of molecular imaging. The physiological parameters, including redox status, pH, presence of enzymes, and hypoxia, can be designed as the stimuli of the activatable probes. However, the success rate of imaging nanoprobes for clinical translation is low. Herein, we critically reviewed the recent advances in nanoparticle-based activatable imaging probes. In addition, the challenges for clinical translation of these nanoprobes are also discussed in this review.

Graphical Abstract

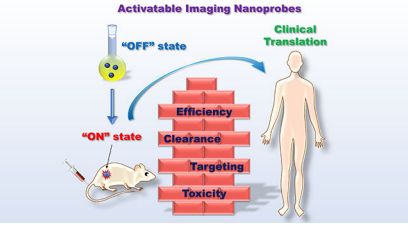

Activatable imaging nanoprobes emit signals only when accumulate in the targeted region, where they respond to the biological or pathological cues, leading to enhanced specificity, sensitivity, and efficacy for molecular imaging. Redox status, pH, presence of enzymes, hypoxia, H_2S, and ATP can be designed as the nanoprobe's stimuli. Herein the recent developments and challenges facing their clinical translation are discussed.

Keywords

nanomaterials; activatable nanoprobe; molecular imaging; theranostics; clinical translation

*Corresponding author: txia@ucla.edu.

1. Introduction

Molecular imaging, which focuses on imaging molecules in living organisms in a non-invasive manner, attracted substantial attention in the past two decades.[1, 2] Beyond structural images, molecular imaging can provide functional and molecular information to understand the mechanisms involved in physiology and disease by non-invasive imaging at the cellular or subcellular level *in vivo*.[3] To achieve these functions, the techniques require two essential elements: (1) the probes whose properties or concentrations can be altered by the specific biological process of interest and (2) a means by which to monitor these probes.

Though most clinical molecular imaging agents are small molecular probes, nanoprobe is a promising candidate to develop a new generation of molecular imaging probes. Compared to the rapid renal clearance of small molecule probes, nanoprobes with proper surface modification usually have a longer blood circulation time.[4, 5] Especially, nanoparticles are preferably accumulated in tumor sites due to their small size and leaky vasculature.[6, 7] Nanoparticles also provide a platform to load functional groups or drugs with a high surface-volume ratio to achieve active targeting and/or drug delivery. In addition, nanoprobes can be designed to have many unique optical and magnetic properties for multi-modal imaging.

The recent advancements in imaging nanoprobes and devices open up additional possibilities in novel imaging techniques such as fluorescence imaging, photoacoustic (PA) imaging, and near-infrared (NIR) II imaging. Optical imaging is emerging as a promising modality for real-time molecular imaging *in vivo* because of its high spatial resolution and high sensitivity. Although attenuation and scattering of light by tissue limit the clinical application, it has been used in small animal models to probe mechanisms involved in many disease processes. Photoacoustic (PA) imaging is an imaging technique that is based on the detection of ultrasonic waves generated by photothermal expansion of light-absorbing tissues or contrast probes under pulsed laser irradiation.[8] Combining the advantages of both ultrasound and optical imaging, PA imaging has the benefits of high spatial resolution, high contrast, and deep tissue penetration (several centimeters).[8] As a fantastic imaging modality, multispectral optoacoustic tomography (MSOT), which can supply reliable anatomy information to the disease theranostics in preclinical trials, has recently attracted considerable attention in biomedical sciences.[9]

Computer X-ray tomography (CT), Single-photon emission computed tomography (SPECT), magnetic resonance imaging (MRI), positron emission tomography (PET), and ultrasound scanners (US) are already powerful tools in clinical settings and are widely used to monitor the molecular probes. Recently, these techniques also have made substantial advancements. Heteronuclear MRI, especially fluorine MRI, is one of the most promising MR techniques owing to the desirable MR properties of the ^{19}F nucleus, lack of endogenous ^{19}F, and good bio-inertness of C-F bonds. The ^{19}F nucleus has a nuclear spin of 1/2, and a gyromagnetic ratio that is 94% of ^{1}H, accounting for an 83% overall signal sensitivity compared to ^{1}H.[10] Chemical exchange saturation transfer (CEST) MRI is another imaging technique that can indirectly detect non-labeled, native molecules by manipulating the water proton signal through selective saturation of exchangeable protons.[11] CEST MRI has now undergone clinical translation for the imaging of dilute biomarkers associated with the

microenvironment as well as administered diamagnetic chemical exchange saturation transfer (diaCEST) contrast agents.[12, 13]

For imaging, the conventional probes typically emit signals continuously under all conditions and develop contrast signals through accumulation at the targeted region, named “always-on” probes. In contrast, the new generation of activatable probes are those in the “off” state at the beginning and switch to the “on” state in the “right” microenvironment of the target tissues or organs. Thereby, activatable probes have a higher signal-to-noise ratio, which can improve sensitivity and specificity for detecting biomarkers or conditions with an imaging modality.

In this review, we will provide a summary of novel strategies on how the activatable probes respond to redox status (Table 1), pH (Table 2), enzymes (Table 3), and other stimuli developed in recent years. The imaging modality includes fluorescence, PA, PET, and MRI. The responsive mechanisms of the activatable nanoprobes were illustrated in Figure 1, which includes redox, pH, hypoxia, enzymes, etc. that will be discussed in detail below. In addition, we will discuss the challenges facing this field and the path forward.

2. Development of smart probes

2.1. Redox responsive probes

Healthy cells and tissues need to maintain a crucial and delicate redox balance between oxidants, including reactive oxygen species (ROS) or reactive nitrogen species (RNS), and antioxidants, including glutathione (GSH), superoxide dismutase (SOD), catalase, cytochrome c, etc.[14] Among them, reduced GSH and oxidized GSH (GSSG) play a major role, and they act in concert with other redox-active compounds to regulate and maintain cellular redox status. The ratio of GSH to GSSG is a major indicator of the redox potential within cells, where an increased GSSG-to-GSH ratio is indicative of oxidative stress. In addition, there are also other redox couples, including NAD(P)H, cytochrome c, thioredoxin, ascorbate, etc. that help to maintain the redox balance.[15, 16] However, in various diseases, the redox state is usually disrupted. Previous studies had revealed that compared to normal tissue, the tumor microenvironment exhibit higher GSH levels[17–19] with overproduced ROS.[20] The abnormal redox balance is also linked with many other pathological conditions, including inflammation[21], diabetes[22], atherosclerosis[23], stroke[24], etc.

2.1.1. Disulfides based redox responsive nanoprobes—Disulfides transform to thiols in the presence of reducing agents, including GSH, and the resulting thiol groups can reversibly re-form disulfide bonds upon oxidation. The mild reaction conditions of thiol-disulfide exchange render it an appealing approach to construct disulfide-containing materials. Disulfides have been incorporated into material systems in the form of disulfide-containing crosslinkers. The cleavage of these crosslinkers leads to the release of the fluorophore to switch on the signal. Zhang et al. developed a multifunctional probe that was consisted of a gold/platinum star-shaped core (Au/Pt star) conjugated with a GSH-sensitive disulfide bond (S-S), a targeting ligand (rHSA-FA), a near-infrared fluorophore (IR780), and glucose oxidase (GOx).[25] As the disulfide linker was cleaved by intracellular GSH, the IR780 molecules could be released for photothermal therapy & photodynamic therapy

(PTT&PDT) as well as bio-imaging. GOx could effectively catalyze intracellular glucose by consuming oxygen to generate H_2O_2 and enhance the local acidity levels. The Pt layer exhibited peroxidase-like property to catalyze H_2O_2, producing toxic •OH to induce oxidative damage in tumors. The probes can simultaneously achieve GSH-sensitive fluorophore release, real-time imaging, and synergetic cancer therapy with PTT/PDT features. Liu et al. conjugated a hydrophobic fluorophore to form a core and linked two hydrophilic polymers that can quench fluorescence by redox-responsive disulfide bonds serving as the corona.[26] The cleavage of disulfide bonds will expose fluorophores to the surrounding proteins at the tumor tissue, leading to fluorescence “turn on” and the release of loaded Docetaxel simultaneously. This redox-triggered light-up nano-micelles offer the opportunity to monitor the pharmacokinetic process of the nano-micellar system and estimate the drug content *in vivo*. The transformed disulfides can also be used to design ROS responsive probes by crosslinking. A GSH-modified, lanthanide-based, fluorescent downconversion nanoparticles (DCNPs), which was in the second near-infrared window (NIR-II), can accumulate in the inflamed area and enhance fluorescence signal intensity due to the GSH oxidation, increased size, and lower excretion rate.[27]

The degradation or self-aggregation of probes can alter the effect on the relaxation rate of water protons to turn the MRI signal “off” and “on” via the disulfide bond cleavage in an abundant GSH microenvironment. Iron oxide nanoparticles (NPs) are excellent T2 contrast agent, and several superparamagnetic iron oxide nanoparticles (SPION) has been approved by the Food and Drug Administration (FDA) for clinical use.[28] The T2 effect of iron oxide NPs is largely dependent on size. Therefore, based on a linker that contains peptides and disulfide bonds, the Gao group developed GSH-triggered NP aggregating systems to increase tumor contrast.[29] In this probe, poly(ethylene glycol) (PEG) ligand was first to bind to Fe_3O_4 NPs surface by a diphosphate group (Figure 2). The maleimide group on the other side of the PEG ligand was used to covalently attach an Arg-Gly-Asp (RGD) peptide and a self-peptide linked through a disulfide bond. After cleavage by the GSH in the tumor environment, the thiol group remaining on RGD moiety crosslinks the particles through interparticle reaction with the remaining maleimide residues from adjacent particles. In situ crosslinking of the responsive probes leads to prolonged retention of particles within tumors and increases the tumor contrast by a factor of more than 3 *in vivo* in contrast to non-crosslinkable Fe_3O_4 nanoprobes. Besides, the single-photon emission computerized tomography (SPECT) imaging capacity is also largely enhanced owing to improved retentions of the crosslinked nanoprobes. The cleavage of disulfides under the reducing environment (e.g., GSH) can also be used to control ^{19}F NMR signal intensity. A “smart” probe that allows GSH-controlled assembly and legumain (Lgmn)-controlled disassembly could turn the ^{19}F NMR signal “off” and later “on” for the sequential detection of GSH and Lgmn. By this design, the probe was successfully applied for the detection of Lgmn activities in zebrafish at low doses (1.5 g/kg) *in vivo* under a high magnetic field strength at 14.1 T.[30] In another example, a self-assembled 1-ICG NP has been prepared with negligible fluorescence, an obvious “off” state. The GSH-induced cleavage would trigger the dissociation of them into ultra-small nanoparticles, leading to the activation of ^{19}F signals. ICG molecules can absorb NIR light to increase the temperature in the microenvironment, which can accelerate the movement of molecules, leading to the complete disassembly of

these loose nanoparticles into small and water-soluble molecules, bringing on a distinct second round of amplification of ^{19}F NMR signals. Signal-to-noise ratio (SNR) of ^{19}F MRI signals observed at the tumor site could be about 3.9 for the first step and reach 8.3 after irradiation with an 808 nm laser at 1.5 W/cm^2 for 6 min.[31] The cleavage of disulfide can even be used to build a redox responsive fluorescence/^{19}F-MRS/^{1}H-MRI triple-functional probe for tri-modality imaging of reducing the biological environment.[32] The probe demonstrated tri-modal detection of reductive biothiol species, with a 70-fold turn-on ratio in fluorescence, a dramatic ~30-fold enhancement in ^{19}F-MRS, and a significant 68% reduction in the longitudinal r1 relaxivity (23.6 ± 0.2 vs. 7.6 ± 0.3 mM^{-1} s^{-1} at 0.5 T).

2.1.2. Metal ions based redox responsive nanoprobes—It is known that Mn-O bonds can fastly biodegrade in the mild reducing microenvironment.[33] Khatik et al. combined Fe_3O_4 and mesoporous silica (SiO_2) that were loaded with Mn^{2+} ions to develop a GSH reactive T1/T2 dual MRI probe.[34] Compared with the control group, the relaxivity value (r1= 5.12 mM^{-1} s^{-1}, r2= 265.32 mM^{-1} s^{-1}) were more than two folds at 3.0 T. Also, based on the Mn-O redox response, Wei et al. constructed a honeycomb MnO_2 nanosponge-sustained autocatalytic DNAzyme (ACD) machine for the robust MRI of the tumor and the concomitant *in vivo* miRNA imaging.[35] The reduction by GSH can also affect the metal optical properties of element nanomaterials. For example, MnMoOX nanorods typically do not have optical absorbance in the NIR window. However, they exhibit strong NIR absorption owing to the reduction of Mo^{VI} in the initial MnMoOx to Mo^{V} by GSH, which triggers the transformation of nanorods to ultrasmall nanodots. Moreover, MnMoOX nanorods with GSH-responsive NIR absorbance could also be employed to achieve tumor-specific PTT.[36] Oxidation-responsive materials mainly target ROS, such as hydrogen peroxide (H_2O_2) and hydroxyl radicals. At mild conditions, H_2O_2 leads to a rearrangement of the oxonium group and the decomposition of the benzopyrylium group while releasing fluorophore.[37] Also, sulfonic esters[38], boronate ester[39], benzil[40], and α-ketoamide moiety[41] can be used to design ROS oxidation-responsive materials.

2.1.3. Nanoprobe with redox-dependent fluorophores—Some fluorophores show redox-dependent absorbance at a certain wavelength, which can be used to construct redox responsive nanoprobes. Based on fluorophores, the Tang group developed a sensitive redox-responsive PA nanoprobe to achieve GSH/H_2O_2 simultaneous detection *in vivo*.[42] Similarly, Ai et al. construct a unique probe to monitor the multispectral optoacoustic tomography (MSOT) signal variations with ROS and RNS-sensitive NIR cyanine fluorophores and upconversion nanoparticles.[43] The probe can track multiple radicals under two independent wavelength channels, and more significantly, precisely validate their complex dynamics and correlations with the redox-mediated pathophysiological procession *in vivo*. They further integrated MSOT with upconversion nanoparticle (UCNP)-mediated luminescence imaging. The spectrum of multiplexing upconversion luminescence (UCL) response and the absorption shift of the H_2O_2-sensitive cyanine dye was deliberately designed to overlap. ROS not only induced a convertible absorption blue-shift of the probe through the chemo-specific reaction, which can be captured by MSOT, but also induced multispectral luminescence changes, which showed the opposite trend of the UCL signal variation comparing with the one observed in MSOT. Thus, the probe provides a spectrally

opposite dual-modal ratiometric output that allows a more sensitive and accurate evaluation of local disease biology and drug treatment responses based on the self-calibrating feature of the reverse-ratiometric PA and UCL imaging technology.[44]

2.2. pH responsive nanoprobe

The intracellular and extracellular pH of normal tissues is kept constant in a range of 7.35–7.45.[45] However, the acid-base balance can be disrupted to complicate the course of widely diverse diseases as well as trauma in many parts of the body. For example, as cancer grows, it rapidly outgrows its blood supply, resulting in a significantly lower oxygen concentration compared with that in healthy tissues, called hypoxia. When tumors are under hypoxia, the upregulation of glycolysis and reduction in oxidative phosphorylation leads to increased lactic acid production, producing an acidic environment in most solid tumors.[46] The pH disruption is also found in the inflammatory processes.[47, 48] Taking advantage of the pH differences under disease conditions, several strategies could be used to design pH-responsive probes.

2.2.1. Reversible protonation process—The pH-sensitivity can be attributed to either the protonation of ionizable groups or acid-cleavage of chemical bonds and result in physical or chemical changes (such as swelling, shrinking, dissociation, and degradation).[49, 50] The protonation of ionizable groups, which is usually reversible, can directly result in optical property changes. Utilizing the reversible protonated process of polyaniline, a broad and pH-responsive ratiometric sensor for PA imaging was developed by loading polyaniline on the surface of Au triangular NPs. The NP was shown to be ultrasensitive to pH, and response time was as fast as 0.6 s and durability as long as 24 h, which was repeatable for longitudinal monitoring.[51] Similarly, a self-assembled charge-transfer nanocomplex, which can accurately respond to pH change in the physiological range, was designed to be a new class of pH-sensitive photoacoustic contrast agent that operates in the NIR-II window.[52] Oxazine-containing polyheterocycles with aggregation-induced emission (AIE) characteristics display remarkable fluorescence changes to protonation and deprotonation. Based on these unique photophysical properties, *in vivo* mapping of intestinal pH of freshwater *Cladocera Moina macrocopa* was achieved, which showed an increased pH gradient approximately from 4.2 to 7.8 along the foregut, midgut, and hindgut.[53]

The protonation can also result in physical changes and indirectly change optical or acoustic properties. Ding et al. developed a luminescence resonance energy transfer (LRET) system using NIR Ag_2S nanodots (NDs) as energy acceptors and UCNPs as energy donors[54]. The protonation and deprotonation of the amino and carboxyl groups on the surface of Ag_2S (NDs), which lead to the combination and dissociation from UCNPs, can efficiently affect the LRET process between UCNPs and Ag_2S NDs. Thus, a ratiometric detection and imaging of pH in tumor cells and zebrafish in NIR windows have been achieved. An acid-induced swelling increases the size of a polymersome-based and perfluorocarbon-encapsulated nanoprobe (from 178 to 437 nm), which can be used for ultrasonic imaging with a lower vaporization threshold for the perfluorocarbon, and eventual release of doxorubicin for deep tissue chemotherapy.[55] Beyond acid-induced size change, the Gao group demonstrated the working mechanism of proton responsive transistor-like

nanoparticles. In addition, based on the transition from positron-emitting neutral copolymer micelles to polycationic polymers, the polymers labeled with the positron-emitting isotope ^{64}Cu can achieve the non-invasive detection of small occult diseases (10–20 mm^3 or 3–4 mm) in the brain, head and neck, and breast by PET imaging.[56]

2.2.2. Acid-cleavage—Acid-cleavage is widely used to construct pH-activatable probes for MRI by releasing metal ions. As Mn^{2+} with five unpaired 3d electrons is known to be a T1-shortening agent, the decomposition of MnO_2 nanoparticles under a mildly acidic environment is widely used to develop pH-activatable probe for MRI. Recently, Yang et al. design a pH-activatable hollow manganese dioxide nano-platform that combines imaging and drug release.[57] This probe could dissemble under reduced pH within the tumor microenvironment (TME) to release loaded therapeutic molecules (chlorine e6 (Ce6) and doxorubicin (DOX)), and in the meantime induce decomposition of tumor endogenous H_2O_2 to relieve tumor hypoxia. As a result, a remarkable *in vivo* synergistic therapeutic effect is achieved through the combined chemo-photodynamic therapy, which triggers a series of antitumor immune responses at the same time. Similarly, MnO_2 as an intelligent "gatekeeper" shield can achieve the controlled release of carbide-glucose oxidase from Fe_5C_2 nanoparticle in the acidic tumor microenvironment. Mn^{2+} could serve as a magnetic resonance imaging (MRI) contrast agent for the real-time monitoring of the treatment process. The generated O_2 and released glucose oxidase in nanocatalysts could effectively exhaust glucose in tumor cells, generating plenty of H_2O_2 simultaneously, which may accelerate the subsequent Fenton reaction catalyzed by the Fe_5C_2 magnetic core in mildly acidic tumor microenvironments.[58]

Comparing with Mn^{2+}, Fe^{3+} is considered much safer. However, designing a Fe^{3+} based activatable agent is problematic, given that the Fe-O-Fe structure of FeIII oxide is hardly breakable at the mildly acidic pH of the tumor microenvironment. Zhang et al. developed a FeIII based activatable probe suitable for releasing FeIII in the tumor microenvironment to enhance MRI and simultaneously improve the treatment of tumors.[59] The UCL nanoparticles were used as a core, and the coordinatively unsaturated FeIII-containing Fe^{3+}/gallic acid complex serves as a shell to construct the probe (Figure 3). At the mildly acidic pH of the tumor microenvironment, FeIII in the nanoprobe can be released due to the unsaturated coordination structure and serves as a photothermal agent. This process can be quantitatively monitored *in vivo* by multiple UCL nanoparticles.

Another iron-based pH-sensitive probe is reported by Li et al.[60] Iron oxide nanoparticle assemblies (IONAs) are crosslinked by the strong small-molecular aldehyde derivative ligands at neutral pH. The cleavage of these ligands in acidic environments lead to the rapidly disassembled IONAs with a significantly enhanced T1 MR contrast. Yi et al. reported self-assembled $NaGdF_4$ and $CaCO_3$ nanoconjugates.[61] In a mildly acidic tumor microenvironment, the embedded $CaCO_3$ nanoparticles generate CO_2 bubbles and subsequently disconnect with the nanoconjugate, releasing the spatial confined Gd^{3+} ions, which shows more than 60-fold contrast enhancement in tumor visualization relative to the commercially used contrast agent Magnevist.

2.2.3. Hydrophobic-to-hydrophilic conversion—The hydrophobic-to-hydrophilic conversion of the pH-responsive polymer is another strategy to develop an activatable probe. At physiological pH, both gadolinium metallofullerene (GMF) and drug molecules are encapsulated into the hydrophobic core of nanoparticles formed by the pH-responsive polymer and shielded from the aqueous environment, resulting in relatively low longitudinal relativity and slow drug release. However, in the acidic tumor microenvironment, the hydrophobic-to-hydrophilic conversion of the pH-responsive polymer leads to amplified MR signal and rapid drug release simultaneously. This prepared activatable MRI contrast agent can not only detect tumors but also monitor drug release.[62]

Wang et al. developed size-switchable nanocapsules that respond to NIR light and the acidic TME. The nanocapsules are stable in the blood with a large initial size. In an acidic microenvironment, the capsules shrink and decompose into smaller ones induced by irradiation of the NIR laser, and DOX will be released. The capsules can also react with endogenous H_2O_2 in tumors and overproduce ROS to overcome the tumor hypoxia-related drug resistance. These active nanocapsules provide dual-modal MRI and fluorescence imaging information with enhanced tumor accumulation.[63]

In summary, there are several strategies to design pH-responsive probes. Currently, most pH-responsive probes are focusing on the tumor due to its acidic microenvironment. It is foreseeable that the same principle could be extrapolated to diagnose and treat other diseases that involve pH disruptions.

2.3. Enzyme responsive nanoprobe

Enzymes play various critical roles in different biological processes. Disease-associated enzyme dysregulations have recently become an emerging target for nanomedicine. Here, we describe several typical enzymatic triggers that could be integrated into the nanoprobe design.

2.3.1. Matrix metalloproteinases (MMPs)—MMPs are closely associated with tumor invasion and metastasis.[64] The upregulated expression of MMPs within the tumor microenvironment can serve as site-specific biological cues for activating bio sensitive materials. This strategy has been applied for the quantitative detection of MMP-2 expression *in vivo.*[65] A NIR dye and a quencher were covalently linked through a peptide substrate of MMP-2 (Figure 4). Upon cleavage with activated MMP-2, this probe presented a dramatic MMP-2 concentration-dependent absorption at around 680 nm, and an MMP-2 concentration-independent absorption at around 730 nm. Using the ratio between the PA signal at 680 nm and 730 nm, this probe can detect MMP-2 expression in breast cancer *in vivo* quantitatively.[66] Enzyme-activated degradation of the gelatin scaffold was also used to release drug and monitor this process simultaneously. The NIR fluorescence was first shielded by satellite CuS NPs and then recovered depending on the amount of chemo-drug doxorubicin released in MMP overexpressed tumor environment.[66] Another article describes a nanoplatform based on MMP-responsive gold nanoparticles (AuNPs). The complementary DNA strands were first attached to the AuNPs' surface. The DOX and PEG were then coated on the particles via a thermal-labile linker and an MMP-cleavable peptide,

respectively. Under the MMP-abundant microenvironment, the PEG layer was rapidly cleaved to expose the complementary DNA strands result in aggregation. This process improved the accumulation of NPs in tumors and induced the redshift of their absorption, which enhanced PA imaging signal and the DOX could be released due to the localized elevation of temperature, serving as photothermal chemotherapy (PTT).[67]

2.3.2. Furin—Furin is a member of the proprotein convertase family, which has a crucial role in tumor progression, metastasis, and angiogenesis.[68] In one study, furin cleavage of a precursor peptide induces self-assembly to form intracellular NPs to enhance tumor microPET imaging, achieving a tumor/liver ratio of 9.1-fold compared with the control.[69] In another study, furin mediated self-assembled NPs not only has a 6.5-fold olsalazine CEST signal but also increase the antitumor therapeutic effect by 5.2-fold compared to olsalazine without furin responsiveness, which showed an excellent "theranostic correlation" (R^2 = 0.97) between the imaging signal and therapeutic response (normalized tumor size).[70]

2.3.3. Phospholipases—Phospholipases also function in the extracellular microenvironment when selected as therapeutic targets.[71] An in situ self-assembled nanoparticle system response to alkaline phosphatase (ALP) was designed for simultaneous enhancements in NIR fluorescence (>70-fold at 710 nm) and r1 relaxivity (~2.3-fold), which achieved real-time, high-sensitivity, high-spatial-resolution imaging and localization of the ALP activity in live tumor cells and mice.[72] Another NIR probe can efficiently be converted to IR775-Phe-Phe-Tyr-OH from IR775-Phe-Phe-Tyr(H_2PO_3)-OH under the catalysis of ALP and enhanced 2.3 folds of the 795 nm PA signal *in vivo* at four hours after NP injection.[73]

2.3.4. Caspases—Caspase-3 and −7 are hallmarks of apoptosis, and they play essential roles in the regulation of cell number and maintenance of tissue homeostasis.[74, 75] The cleavage of peptides by caspase-3/7 promotes the dynamic response of the nanoprobe to the caspase-3/7 activity, which allowed ^{19}F MRI of caspase-3/7 activity in living mice for the first time using a PFC-encapsulated ^{19}F MRI nanoprobe with off/on-switching ability.[76]

2.3.5. Other enzymes: Intracellular hyaluronidase can be used as a tumor target. A core-shell nanostructure was designed with UCNPs as a core and fluorophore-doped degradable microporous silica as the shell for protein delivery. On top of that, a hyaluronic acid (HA) shell was synthesized on the surface. The HA shell of this core-shell structure could be hydrolyzed by hyaluronidase in tumor cells. Without the protection of the HA shell, the silica shell then began degradation and caused the release of the proteins. The spectral overlaps between UCNPs and silica shell can be used to track protein delivery *in vivo* via NIR luminescence. The probe successfully helped us to understand where, when, and how therapeutic proteins take effect *in vivo.*[77]

The condensation reaction between 6-hydroxy-2-cyanobenzothiazole (CBT) and cysteine has been shown for various applications such as site-specific protein labeling and *in vivo* cancer imaging. Chen et al. further expands the substrate scope of this reaction by varying the substituents on aromatic nitriles and amino thiols, thus develop a general system for imaging hydrolytic enzymes. They identified the minimum structural requirement to form

nanoparticles through the macrocyclization and assembly process. Also, they designed fluorescent probes consist of 2-pyrimidinecarbonitrile and cysteine joined by a benzyl linker to image caspase-3/7 and b-galactosidase activity in live cells.[78]

2.4. Hypoxia responsive nanoprobe

Hypoxia, an absence of adequate oxygen, is associated with various diseases, including cardiomyopathy, ischemia, rheumatoid arthritis, acute and chronic vascular disease, pulmonary disease, and cancer.[79–81] Specifically, hypoxia is common in most solid tumors resulting from the imbalance between the high oxygen consumption and the poor oxygen supply, which because of the rapid proliferation of tumor cells and enhanced angiogenesis, respectively. Compared with normal tissue molecular oxygen (O_2) level (2% ~ 9%), "hypoxia" tumor microenvironment only has a O_2 levels of 0.02% ~ 2% (<2.5 mmHg pO_2). [79, 82] Tumor hypoxia is generally considered negative for prognosis because of its central role in tumor progression and resistance to therapy.

There are two main strategies to prepare hypoxia activable nanoprobes. One is based on hypoxia or oxygen responsive groups, including nitroaromatic derivatives, azobenzene, polypyridyl, pyrenyl units, and transition metal complexes. Another one is the indirect imaging based on the biomarkers induced by hypoxia. Hypoxia-inducible factor-1α (HIF-1α) is a crucial transcription factor that is induced by hypoxia, which can be used as the target for indirect hypoxia imaging.[83, 84] Here, we only focus our discussion on hypoxia-responsive groups in nanoprobe design.

Nitroaromatic derivatives that can be converted to hydrophilic 2−aminoimidazole under hypoxic conditions with relatively high sensitivity are among the most widely exploited functional motifs. By incorporating a nitrobenzene-substituted BODIPY, which can be activated by reductive enzymes, especially nitroreductase (NTR), the probe obtained 55-fold fluorescence enhancement with the limit of detection as low as 7.08 ng/mL. *In vivo* imaging of hypoxia in a murine model of myocardial ischemia was achieved by the nanoprobe with high sensitivity and excellent biocompatibility.[85] Similarly, azobenzene, another well-established hypoxia sensitive motif previously used as an imaging probe, has been incorporated in a ratiometric surface-enhanced Raman scattering (SERS) nanoprobe for imaging hypoxic living cells or tissues.[86] The azoalkynes, which have alkyne Raman bands at 2207 cm^{-1}, were assembled on a single-walled carbon nanotube (SWCNT) surface-functionalized with Ag/Au alloy nanoparticles for the first time. In the hypoxia tumor microenvironment, azoalkynes would be reduced and removed from the surface. While SWCNT shows a strong Raman signal at 2578 cm^{-1}, which can be used as the internal standard. Thus, the hypoxia level can be determined by the ratio of two peak intensities (I_{2578}/I_{2207}).[86]

Li et al. developed NIR excited nanosensors, in which the donor and acceptor pairs within a biological metal-organic framework (bio-MOF) matrix is precisely controlled to enable upconversion fluorescence resonance energy transfer (FRET). It is suggested for detecting the O_2 concentration inside tumors with reduced signal disturbance and health detriment. Under NIR excitation, as-fabricated core/satellite nanosensors exhibit improved FRET efficiency and reversible hypoxic response with high sensitivity, which are effective both *in*

vitro and *in vivo* (zebrafish) for cycling normoxia-hypoxia imaging. The FRET core/satellite nanostructures, in which tris(4,7-diphenyl-1,10-phenanthroline) ruthenium(II) dichloride ($[Ru(dpp)_3]^{2+}Cl_2$) as the quenchable indicator for O_2 with a linear Stern-Volmer relationship, UCNPs as antennas convert NIR light into the visible light absorbed by the $[Ru(dpp)_3]^{2+}Cl_2$, have been used for *in vivo* non-small-cell lung lesion tracking in a genetically engineered murine model. It allowed optical hypoxia monitoring without apparent long-term biotoxicity.[87]

Zheng et al. reported a new ratiometric hypoxia luminescent imaging (RHyLI) nanoprobe based on semiconducting polymers and phosphor that can exhibit dual NIR emissions (685 and 795 nm) under the red light (up to 650 nm) excited. The phosphorescence emission at 685 nm is inert to oxygen level. While the emission at 795 nm would increase to 13.5-fold when the oxygen level dropped to 0 from 21%. Thus, the ratio of the emission intensity between 795 and 685 nm (R795/685) increased nonlinearly as the oxygen level decreased, with the sharpest response in the low oxygen range. These results showed the nanoprobe could efficiently penetrate the hypoxic regions of the tumor tissues after systemic administration and allow for quantitative imaging of tumor hypoxia dynamics during radiotherapy over one week.[88]

2.5. Hydrogen sulfide responsive nanoprobe

Hydrogen sulfide (H_2S) is a highly reactive endogenous signaling molecule, playing a critical role in diverse physiological functions. Aberrant concentration and tissue distribution of H_2S are associated with many diseases (e.g., liver inflammation, hypertension, diabetes, and cancers). Therefore, precise spatiotemporal detection of H_2S in living subjects is essential to the study of the biological functions and accurate diagnosis of H_2S related diseases.

In the presence of H_2S, the boron-dipyrromethene dye could generate the NIR-II emission. Combined with another dye, which is inert to H_2S, the probe can precisely detect H_2S by ratiometric imaging.[89] The boron-dipyrromethene dye can also be used to construct H_2S-activatable NIR photothermal agents for imaging-guided and photo controlled drug release.[90]

H_2S may serve as a strong reductant capable of fast donating electrons to certain organic **π**-electron structures and induced color changes during this electron-transfer process. For example, the strong absorption (between 500 and 850 nm) of dicationic 1,1,4,4tetraarylbutadiene would dramatically decrease due to the reduction. By doping this dye into semiconducting polymer nanoparticles, sensitive, non-invasive, and real-time detection of hepatic H2S levels in mice was achieved.[91] The researchers further optimized the structure of this dye to improve reaction kinetics toward H_2S with longer absorption wavelength (Figure 5). The final probe displays a fast reaction rate ($1563 \pm 141\ M^{-1}\ s^{-1}$) and a large afterglow turn-on ratio (~122-fold) toward H_2S, enabling high-sensitivity and specificity measurement of H_2S concentration in blood from healthy persons, hepatic or colorectal cancer patients.[92]

2.6. Adenosine 5'-triphosphate responsive nanoprobe

Adenosine 5'-triphosphate (ATP), referred to as the "molecular unit of currency" of intracellular energy transfer, was found to accumulate at high levels in inflammatory and tumor sites.[93–96]. Thus, ATP can serve as an attractive trigger for activatable imaging.

Li group designed a NIR light-activated DNA nanodevice for sensing ATP in living cells.[97] In this nanodevice, oleic acid-capped $NaGdF_4$:70%Yb,1%Tm@$NaGdF_4$ UCNPs (40 nm) were synthesized with a thermal decomposition approach to achieve high efficiency of NIR-to-UV conversion. The ATP aptamer strand modified with a fluorophore Cy3 and the quencher-bearing a photocleavable (PC) group was initially formed a complementary DNA. FRET occurred between Cy3 (or Cy5 for *in vivo* imaging) and quencher, resulting in the "off" state of fluorescence. After UCNPs convert NIR light to UV light, the photolysis of the PC group generates short DNA fragments. In this condition, the aptamer will restore its capability to switch its structure to bind ATP, leading to the dissociation of the DNA probe and the recovery of the Cy3 fluorescent signal. By introducing the pH (low) insertion peptide (pHLIP) into this DNA nanodevices, the spatially controlled imaging of ATP in the acid extracellular milieu of tumors with ultrahigh signal-to-background ratio was achieved.[98] Combining with gold nanoparticle (AuNP) with polyethylene glycol (PEG), this DNA nanodevice can further be used for bioimaging and photodynamic therapy.[99].

Chen group engineer the self-assembled quantum dots (QDs)-phenolic nanoclusters for ATP-responsive imaging and drug release. The hydrophobic core-shell structured CdSe@ZnS QDs (~9.8 nm) was assembled into nanoclusters linked by tannic acid (TA), with diameters of 55 nm. ATP could compete with TA and partly displace TA to bind on the QDs surface, leading to the disassembly of the nanoclusters and the enhancement of the fluorescence intensity.[100]

2.7. Multi-stimulants responsive nanoprobe

We have summarized many smart probes that respond to a certain stimulus or condition. While in many cases, there is more than one condition can be used as the trigger. For example, redox, hypoxia, low pH, and some overexpressed enzymes are common in most solid tumor microenvironment, which can all be used to stimulate the smart probes.[46, 79, 101] A deliberately designed probe can achieve dramatically signal increase based on multi-stimulation signals.

For example, the release of metal ions in the acidic environment can be combined with other strategies. A core-shell-structured iron carbide (Fe_5C_2@Fe_3O_4) nanoparticles (NPs) can respond to acidity and overproduction of H_2O_2 in the tumor environment, which effectively inhibits the proliferation of tumor cells through the catalysis of the Fenton reaction.[102] In acidic environments, the released ferrous ions decrease the T2 signal and enhance the T1 signal in MRI, and this T2/T1 switching process provides the visualization of ferrous ions release and ROS generation for the monitoring of tumor treatment process. For another example, a nanoparticle sensor is composed of acetylcholine catalyzing enzymes and pH-sensitive gadolinium contrast agents modified onto the surface of the particles, which can be used to specifically detect acetylcholine in the living brain. The enzymatic hydrolysis of

acetylcholine leads to a localized decrease in pH, which is detected by the pH-sensitive gadolinium chelate. The concomitant change in 1/T1 *in vitro* saw a 20% increase from 0 to 10 μM acetylcholine concentration.[103] In addition, the thermo- and pH-responsive copolymers of poly(N-isopropylacrylamide) and poly(acrylic acid) were used to design core/shell hydrogel NPs. In the range from 10 to 80°C, the photoluminescence intensities of the NPs show linear response depend on temperature. In the range from pH6.5 to pH7.6, the blue emission of the NP's shell is linear depend on pH with a resolution of 0.1 unit, while the red emission is inert to pH changes.[104]

The weak electron acceptor (benzo[c][1,2,5]thiadiazole-5,6-diamine) can be oxidized by NO in acidic conditions to form a stronger acceptor (5H-[1,2,3]triazolo[4,5-f]-2,1,3-benzothiadiazole), which significantly increased the molecule absorption in the NIR region. Based on this transformation, a dual-stimuli-responsive theranostic nanoprobe was developed for simultaneously activatable cancer imaging and photothermal therapy. Under NO and acidity dual stimuli, the PA signal is 9.8 times and 132 times higher than that of NO and acidity alone, respectively.[105] Moreover, the poly(ethylene glycol)-conjugated iridium (iii) complex, a NIR probe, was developed to respond to both tumor acidity and hypoxia, which is akin to the cascade amplification of signals in electronics. In the presence of the first targeted physiological stimulus, the probe gets converted to a secondary form (the reporter). In the presence of a second targeted stimulus coupled to the first stimulus, the signal of the reporter is amplified and can be observed in a different readout channel. Such signal amplification involves the propagation of signals from the precursor to the reporter, which will lead to improved detection sensitivity.[106] Based on a multispectral upconverting nanophosphor ($NaYF_4$: Yb, Er, Tm) as the luminescence resonance energy transfer donor, a GSH-sensitive dye and an H_2O_2-sensitive dye as the acceptors, a ratiometric nanoprobe was developed for real-time and synchronous monitoring of the variation of GSH and H_2O_2 *in vitro* and *in vivo*.[107]

The multi-stimulation design not only can magnify the signals but also can be used to research the correlation between these abnormal characteristics. Gao group design a probe based on a FRET system comprised of Fe_3O_4 nanoparticles, pH-sensitive ratiometric fluorescent dye, NIR dye, MMP-9 specific peptide substrate linker, and folic acid as a tumor active targeting moiety (Figure 6). The fluorescence of a ratiometric pH dye, N-carboxyhexyl derivative of 3-amino-1,2,4-triazole fused with 1,8-naphthalimide (ANNA), is quenched while attached to the surface of a Fe_3O_4 nanoparticle, representing the "off" state. Upon cleavage of the peptide linker by MMP-9, the fluorescence of ANNA is activated, representing an "on" state, which has been previously demonstrated for *in vivo* pH mapping of tumor xenografts after intratumoral injection.[108] By labeling this probe with the NIR fluorescent dye Cy5.5, which is always in an "on" state, the constant Cy5.5 emission and MMP-dependent fluorescence from ANNA can be combined to map MMP-9 activity across the entire tumor quantitatively. The probe can serve as a non-invasive tool to map multiple tumor-associated signatures simultaneously to determine tumor heterogeneity, correlate abnormal characteristics with metastatic potential, and potentially help predict tumor progression and design optimal treatment strategies.[109]

3. Clinically approved nanoparticles

Though a large number of imaging nanoprobes have been designed and reported every year, few of them have been applied in clinical practice. Currently, the clinically approved nanomaterials are mainly MRI and SPECT contrast agents. MRI form pictures by detecting the relaxation signals of (water) proton spin in the strong magnetic field excited by radiofrequency waves. The proton spins return to their equilibrium states via two independent relaxation processes of T1 (spin-lattice) and T2 (spin-spin). The chemical agents that can accumulate the recovery of these two relaxations are called T1 contrast agents and T2 contrast agents, respectively. Though MRI is a powerful tool to image anatomical structures or blood flow, the sensitivity to differentiate between healthy and unhealthy tissue remains to be improved by using the contrast agent. The most commonly used intravenous contrast agents are T1 contrast agents, which are based on gadolinium chelates.[5] For example, Gd-DTPA (diethylene triamine pentaacetate acid, DTPA) can be used to help to image the breast, spine, liver, heart, brain, the soft tissue of joints, and inside bones.[110–112] Some studies have pointed out the concern of gadolinium-associated nephrogenic systemic fibrosis (NSF) [113], and the FDA has issued warnings to limit the usage of gadolinium-based contrast agents in patients with renal failure.[114] In addition, the FDA expressed concerns on gadolinium retention in patients' bodies, including the brain, for months to years after receiving these drugs. However, the FDA has not identified adverse health effects from retained gadolinium in the brain.

As a safer alternative, SPION has received considerable attention due to their excellent T2 effect. The first clinically available brand is Feridex®/Endorem® (ferumoxide), a colloidal SPION associated with dextran, which was approved by the FDA in 1996 as a T2 contrast agent. Then, Resovist®/Cliavist® (Ferucarbotran), SPION coated with carboxydextran, is approved in the European market. However, these two T2 contrast agents are discontinued now due to a lack of clinical users. Combidex®/Sinerem®/Ferrotran® (Ferumoxtran-10) is an ultrasmall superparamagnetic iron-oxide (USPIO) coated with dextrans, which is still undergoing clinical trials. However, a pivotal study failed to demonstrate a consistent and statistically significant benefit for sensitivity that confirm non-inferiority concerning specificity; therefore, their clinical development was stopped. Feraheme®/Rienso® (ferumoxytol) is a USPIO, which is FDA-approved for intravenous iron-replacement therapy in anemic patients with chronic kidney disease. Interestingly, the paramagnetic properties of ferumoxytol also allow it to be used as an MRI contrast agent.

The colloidal NPs, such as sulfur and stannous fluoride, are widely used to carry radioisotope to enhance SPECT imaging. ^{99m}Tc is the most common radioisotope. Sulfur colloid (Technecoll®), albumin nanocolloid (Nanocoll®), rhenium sulfide nanocolloid (Nanocis®), and tin colloid (Hepatate®) have been approved for clinical practice. The intravenous nanoparticles that are currently undergoing clinical trials are summarized in Table 4. The imaging model of these nanoprobes includes MRI/US, MRI, PET/MRI, PET, SPECT/CT, and optical imaging. None of them is an activatable probe.

4. Challenge of smart probes

Toxicity concerns of nanoparticles are non-negligible, which have led to their limited clinical translation to date. Systematic evaluation of the toxicity and metabolic behavior of nanomaterials in the body is essential to impel their clinical transition and extend their applications in disease theranostics. Ideally, the probes should accumulate in the targeted tissues or organs, and have higher sensitivity and intensity with the low side effect. After imaging, these probes should be cleared quickly and safely. This is a non-trivial task, and here are some of the major challenges.

4.1. Targeting

Tumor imaging with or without treatment modality is a major use of nanoprobes. For tumor imaging, there are two strategies for nanoprobes to accumulate the target region: active targeting and passive targeting. Active targeting can be achieved by using specific ligands (antibodies or peptides) that can be grafted to the nanoparticle surface and specifically bind to overexpressed receptors at the target site. The enhanced permeability and retention (EPR) effect is well known as the passive targeting mechanism. This effect based on two factors: 1) heavy energy and oxygen demand in fast-growing tumors leads to extensive angiogenesis and hyper-permeabilized neo-vasculatures, which cause leakage of circulating macromolecules and small particles; and 2) the lack of effective lymphatic drainage system in the tumor, which leads to the macromolecule or nanoparticle accumulation. In the last decade, the EPR effect was considered to be the main mechanism to overcome the lack of targeting of traditional small molecule drugs.

However, after more than 30 years since the discovery of the EPR effect, the clinical evidence of the EPR effect is largely missing. The success rate of nanomedicine clinical translation for cancer treatment is low despite some successes such as Doxil, Abraxane, and Vyxeos. Less than ten anticancer drug delivery systems and imaging nanoprobes (e.g., silica-based Cornell dot, gold-based Auroshell) are currently in phase III or IV clinical trials, and only ten have received regulatory approval in Europe and the United States, seven of which are liposomal formulations. This is primarily due to the poor delivery efficiency of nanoparticle formulations to the cancer site. Recent studies showed the EPR effect is dependent on tumor types, while fast-growing tumors such as carcinomas are very vascular and therefore have more porous/leaky blood vessels; slow-growing tumors such as sarcomas are not extremely vascular.[115] However, this still needs to be verified in humans. Recently, original research revealed that the dominant mechanism of gold nanoparticle transport in the tumor is an active process and not a passive process such as EPR. In this study, the frequency of endothelial gaps in the tumor vasculature of the U87-MG glioblastoma xenograft model, the supposed sites where EPR happens, was analyzed using TEM and three-dimensional (3D) microscopy. Based on mathematical modeling using 3D images of tumor vasculature, and measuring the accumulation of nanoparticles in tumors post-intravenous injection, they found that the number of gaps observed via TEM is not sufficient to explain the accumulation of nanoparticles in tumors. They found trans-endothelial pathways are the dominant mechanism of nanoparticle extravasation into tumors. This has been validated in an additional three different mouse models and three different types of

human tumors. This study is especially relevant to nanoprobes that are mainly inorganic nanoparticles. However, we have to keep in mind that substantial differences exist among tumor types, anatomical locations, and stages from patient to patient, and one also needs to consider that escaping the systemic circulation into the tumor is only one of many barriers faced by cancer nanomedicines, *e.g.*, high intratumoral pressure and dense extracellular matrix. Nevertheless, these results challenged our current rationale of using EPR effects to develop cancer nanomedicine and suggest that understanding these active pathways will unlock strategies to enhance tumor accumulation.[116]

Although the clinical demonstration of the EPR effect is still required, recent advances help us to design smart probes for clinical settings. In addition to consideration of passive targeting such as EPR effects, the active targeting strategy should be considered. Typically, antibody, peptide, folic acid, transferrin, etc. are put on the surface of the nanoprobe for active targeting ability. This needs to consider the effect of the protein corona, which may affect active targeting. When NPs are introduced into the physiological environment, unspecific adsorption of proteins will form a layer on the particle surface, named “protein corona” (PC).[117] The PC is highly dynamic, and it is dependent on the characteristics of the NP (i.e., size, charge, and surface engineering), proteins (i.e., molecular weight, isoelectric points, structure, and folding), conditions (i.e., time, temperature, concentration), and type of biological sample (i.e., plasma, urine, tissue lysate, etc.). Proteins in the PC also vary under individual disease states (e.g., diabetes, rheumatism, cancer, obesity, hemodialysis, hyperfibrinogenaemia, hypercholesterolemia, hemophilia, and pregnancy), as well as specific disease conditions (e.g., cancer stage or grade and tumor heterogeneity). For nanoprobes, PEG is typically used to reduce the binding of opsonins and proteins and prolong the circulating time, and currently is the most common strategy to reduce PC formation and aggregation. In addition, zwitterionic polymers are other alternatives for reducing PC formation. Beyond compromising the targeting efficiency of NPs, PC also can be used to achieve active targeting. By modifying the liposomal surface with a short nontoxic peptide, the NPs obtained specific interactions with apolipoproteins. After adsorption of plasma apolipoproteins, the PC exposed the receptor-binding domain of apolipoproteins to achieve brain-targeted delivery.[118] In general, understanding and control the PC rather than eliminate that provides a new impetus for active targeting.

4.2. Clearance

The clearance of nanoparticles follows two main pathways in metabolic processes: 1) urinary excretion and 2) hepatobiliary and feces excretion.[119, 120] Nanoparticles with sizes exceeding 6 nm could be rapidly taken up by the RES (liver and spleen). Nanoparticles with small sizes (<5.5 nm) are quickly excreted in the urine by the kidney because their sizes fall below the threshold required for kidney filtration.[121] Some nanoparticles with large sizes could be cleared by the kidneys after their degradation during the prolonged circulation in the body.[122]

However, the clearance of NPs in a broad sense is very complicated. It is associated not only with the size of the particles but also with surface modification. The solution synthesis of colloidal NPs requires suitable surface capping agents to prevent the NPs from

uncontrollable growth, and at the same time, increase the colloidal stability of the NPs. Towards biomedical applications, biocompatible surface coatings are required not only for colloidal stability in physiological environments but also provide reactive groups to further couple bioligands to enhance the accumulation of the particle probes in the region of interest. Surface coatings will inevitably interact with biomolecules such as lipids, sugars, and especially proteins that may subsequently adsorb onto the surface of NPs to form the PC, as we mentioned above. PC may affect the clearance of them from the mononuclear phagocyte system.

Inorganic nanoparticles, especially gold nanoparticles, are non-biodegradable and are stable enough as a study object to understand the clearance of nanoparticles *in vivo*. Using a series of GS-AuNPs with different core sizes (2.5 nm and 1.7 nm NPs and atomic precisely sub-nanometer clusters), Du et al. found that the glomerular filtration barrier can behave as an atomically precise bandpass filter to significantly slow down the renal clearance of smaller particles in the sub-nanometer size regime while maintaining the renal clearance at a comparable level in the range of 1–3 nm.[123] They found that Au nanoclusters (AuNCs) smaller than 1 nm showed a decrease in renal clearance efficiency. This is because smaller AuNCs are more easily and physically retained by the glycocalyx of the glomeruli, similar to the separation principle used in gel filtration or size-exclusion chromatography.

In another study, polyethylene glycol-block-poly(ε-caprolactone) (PEG-PCL) and PEG-block-poly(D, L-lactide) (PEG-PDLLA) micelles were used to evaluate the blood clearance kinetics.[124] A pair of FRET dyes, Cy5 and Cy5.5, was conjugated to the polymer to obtain PEG-PCL-Cy5 and PEG-PCL-Cy5.5. When these two polymers were assembled to micelles, a strong FRET effect would occur. In contrast, the disassembly of the micelles led to the low efficiency of FRET. *In vivo* experiments demonstrated that bloodborne proteins (particularly albumin) induced the most (~80%) PEG-PCL and PEG-PDLLA micelles to quickly dissociate into unimers, which were sequestered by Kupffer cells, while intact micelles were difficult to be cleared.

An active nanoprobe for MRI was also used to study renal clearance. Tang group developed monodisperse Fe_2O_3 supraparticles, which are self-assembled 3–5 nm-sized Fe_2O_3 NPs. The carboxyl groups of citrate molecules among the nanocrystals played an essential role in the self-assembly. In the presence of GSH and H^+, the disassembly and degradation of supraparticles increase r1 value (from 0.19 to 1.20 mM^{-1} S^{-1}) and decrease r2/r1 value (from 20.79 to 1.59). After intravenous tail vein injection, the intensity of MRI signals at the kidneys and liver is enhanced in 10 min and almost completely recover after twelve hours. The MRI signals at the bladder could be detected at the same time as that at the liver and kidneys; however, the intensities are much higher than that of the two organs. The results demonstrated that the Fe_2O_3 supraparticles are mainly excreted by renal clearance.[125]

Overall, the development of rapidly cleared nanoparticles is an important task that needs to be adequately explored for biomedical applications, especially for the translation of such nanoprobes into clinical trials. In addition to the sensitivity and specificity, the clearance of the activatable nanoprobes should be paid more attention. Conversely, these activatable probes may also provide a powerful tool to understand clearance behavior.

4.3. Toxicity

The clearance of nanoparticles from the blood vessel is the end of the imaging agent but not the end of nanomaterials. 90% of intravenously administered radio-labeled fullerenes are retained for at least a week, with 97.0% lodging in the liver and spleen. The toxicity of these materials should be considered before they were mostly excreted.

In addition to activatable nanoprobes, numerous new nanomaterials are designed and produced continuously with novel physicochemical properties. Few have been evaluated for their toxicity systemically. The toxicity of nanomaterials can be attributed to the chemical composition, size, shape, surface coating, which are accompanied by different surface energy, redox status, surface defects, charge. Over the year, we have studied the toxicological profiles of metal oxide nanoparticles including transition-metal oxides (TMOs, e.g., Co_3O_4, Mn_2O_3) versus rare-earth oxide (REO) NPs (e.g., Gd_2O_3, Y_2O_3) and identified their toxicity mechanisms as well as the structure-activity relationships (Figure 7).[126] For example, MOx with a high dissolution rate (ZnO, CuO, V_2O_5, etc.) could shed toxic ions to induce oxidative stress, inflammatory cytokines, and cell death. TMOs with conduction band energy overlapping the biological redox potential could induce oxidative stress and apoptotic cell death by inducing the activation of caspases 3 and 7. In contrast, REOs could transform into sea urchin structures in the acidic environment of lysosomes after cellular uptake, which triggers lysosomal damage and activation of the NLRP3 inflammasome, production of IL-1β, and GSDMD-mediated pyroptosis in macrophages, with cell swelling, membrane blebbing, and increased membrane permeability. High aspect ratio MOx could also trigger lysosomal damage and NLRP3 inflammasome activation, which can lead to chronic lung inflammation and fibrosis. Fumed silica mostly attaches to the cell membrane, causing membrane perturbation and potassium efflux, which lead to NLRP3 inflammasome activation and IL-1β production. MOx with cationic surface coating could induce proton sponge effects in lysosomes after cellular uptake, which can trigger cell death.[126–129]

For toxicity evaluations of nanoprobes, it is recommended to use the mechanisms-based high-throughput screening (HTS) and a predictive toxicological approach, which will make predictions on the physicochemical properties of nanomaterials that may result in pathology or disease *in vivo*.[130] To establish this approach, four elements are essential: 1) a well combinational nanoparticle library, 2) rigorous physicochemical characterizations of nanomaterials, 3) development of *in vitro* HTS approaches to assess biological effects of nanomaterials quantitatively, 4) establishment of quantitative structure-activity relationships (SAR) with *in vivo* results.[131] In this predictive toxicological paradigm, HTS will be used to achieve rapid hazard ranking among a batch of nanoprobes.[128, 129, 132, 133] The cells will include epithelial cells, endothelial cells, liver cells including Kupffer cells and hepatocytes, etc. The parameters will include oxidative stress, inflammatory cytokine production, DNA damage, and cell death. The *in vitro* HTS results will be validated *in vivo* in rodent animal models. The results from the *in vitro* and *in vivo* studies will be used to build nanomaterial structure and activity relationships (nano-SAR), which is helpful to design safer nanoprobes for biomedical applications.[126, 131, 134–136]

5. Conclusion

In this review, recent achievements on activatable molecular imaging nanoprobes, especially for tumor-associated microenvironment detection, including optical imaging, MR imaging, and PA imaging, were summarized. Compared with small molecular imaging probes, nanoprobes are considered as a promising platform to design responsive mechanism upon different stimuli, including hypoxia, acidic condition, specific enzymes, redox status, etc., because their large specific surface area offers a big room to modify their functional moieties. Although a large number of achievements have been reported in this area, considerable challenges remain in the development of activatable nanoprobes for imaging *in vivo*. For example, redox responsive nanoprobes could be expanded beyond GSH/GSSG to other redox couples for nanoprobe design.[15, 137] This will facilitate the diagnosis and/or therapy not only for the tumors but also for inflammation and other diseases with high specificity and sensitivity. Furthermore, hypoxia is increasingly recognized to play critical roles in the pathogenesis of other major causes of mortality, including myocardial ischemia, metabolic diseases, chronic heart and kidney diseases, and reproductive diseases such as preeclampsia and endometriosis. It is expected more nanoprobes will be developed for diseases other than tumors, which will allow us to understand the etiology and develop treatments. Also, for enzyme responsive nanoprobes, due to the vast number of enzymes that play important roles in many disease processes, there is a lot of room to design new enzyme-responsive nanoprobes, which will facilitate the diagnosis and treatment of a wide variety of diseases in the future. In addition, because the progression of diseases including tumors is associated with multiple physiological factors in the microenvironment, designing multi-modal nanoprobes are meaningful for fundamental studies and clinical applications. Although studies have demonstrated the potential application of stimulus-responsive imaging nanoprobes in the clinic, including the image-guided surgery, drug control release, evaluating therapeutic efficacy, and photothermal therapy, continued efforts are still needed to develop strategies for targeted delivery, incorporating anticancer agents with the nanoprobes, and constructing multi-stimuli responsive smart diagnostic and theranostic nanoplatforms. Finally, the toxicity evaluations and structure-activity relationships should be carried out to predict the potential adverse outcomes and facilitate the clinical translation of these nanoprobes.

Acknowledgments

Supports are from NIEHS U01 ES027237, NHLBI R01 HL139379, and UCOP LFR-20-651032 as well as HNSF 182300410374.

References

[1]. Herschman HR, Science 2003, 302, 605. [PubMed: 14576425]
[2]. Weissleder R, Nature Reviews Cancer 2002, 2, 11. [PubMed: 11902581]
[3]. Weissleder R, Mahmood U, Radiology 2001, 219, 316. [PubMed: 11323453]
[4]. Liu C, Hou Y, Gao M, Advanced Materials 2014, 26, 6922. [PubMed: 24616057]
[5]. Gao Z, Ma T, Zhao E, Docter D, Yang W, Stauber RH, Gao M, Small 2016, 12, 556. [PubMed: 26680328]
[6]. Duncan R, Nature Reviews Drug Discovery 2003, 2, 347. [PubMed: 12750738]

[7]. Jain RK, Annual Review of Biomedical Engineering 1999, 1, 241.

[8]. Weber J, Beard PC, Bohndiek SE, Nature Methods 2016, 13, 639. [PubMed: 27467727]

[9]. Ntziachristos V, Razansky D, Chemical Reviews 2010, 110, 2783. [PubMed: 20387910]

[10]. Xie D, Yu M, Kadakia RT, Que EL, Accounts of Chemical Research 2020, 53, 2. [PubMed: 31809009]

[11]. Ward KM, Aletras AH, Balaban RS, Journal of Magnetic Resonance 2000, 143, 79. [PubMed: 10698648]

[12]. Jones KM, Pollard AC, Pagel MD, Journal of Magnetic Resonance Imaging 2018, 47, 11. [PubMed: 28792646]

[13]. Xu X, Yadav NN, Knutsson L, Hua J, Kalyani R, Hall E, Laterra J, Blakeley J, Strowd R, Pomper M, Barker P, Chan K, Liu G, McMahon MT, Stevens RD, van Zijl PCM, Tomography 2015, 1, 105. [PubMed: 26779568]

[14]. Andreyev AY, Kushnareva YE, Starkov A, Biochemistry (Moscow) 2005, 70, 200. [PubMed: 15807660]

[15]. Ying W, Antioxidants & Redox Signaling 2008, 10, 179. [PubMed: 18020963]

[16]. Cook JA, Gius D, Wink DA, Krishna MC, Russo A, Mitchell JB, Seminars in Radiation Oncology 2004, 14, 259. [PubMed: 15254869]

[17]. Kuppusamy P, Li H, Ilangovan G, Cardounel AJ, Zweier JL, Yamada K, Krishna MC, Mitchell JB, Cancer Research 2002, 62, 307. [PubMed: 11782393]

[18]. Russo A, DeGraff W, Friedman N, Mitchell JB, Cancer Research 1986, 46, 2845. [PubMed: 2421885]

[19]. Perry RR, Mazetta J, Levin M, Barranco SC, Cancer 1993, 72, 783. [PubMed: 8392905]

[20]. Ishikawa K, Takenaga K, Akimoto M, Koshikawa N, Yamaguchi A, Imanishi H, Nakada K, Honma Y, Hayashi J-I, Science 2008, 320, 661. [PubMed: 18388260]

[21]. Tabas I, Glass CK, Science 2013, 339, 166. [PubMed: 23307734]

[22]. Kaneto H, Katakami N, Matsuhisa M, Matsuoka T.-a., Mediators of inflammation 2010, 2010.

[23]. Griendling KK, FitzGerald GA, Circulation 2003, 108, 1912. [PubMed: 14568884]

[24]. Allen CL, Bayraktutan U, International Journal of Stroke 2009, 4, 461. [PubMed: 19930058]

[25]. Zhang A, Zhang Q, Alfranca G, Pan SJ, Huang ZC, Cheng J, Ma Q, Song J, Pan YX, Ni J, Ma LJ, Cui DX, Nano Research 2020.

[26]. Liu XG, Wu M, Hu QL, Bai HZ, Zhang SQ, Shen YQ, Tang GP, Ping Y, Acs Nano 2016, 10, 11385. [PubMed: 28024380]

[27]. Zhao MY, Wang R, Li BH, Fan Y, Wu YF, Zhu XY, Zhang F, Angewandte Chemie-International Edition 2019, 58, 2050. [PubMed: 30589175]

[28]. Qiao R-R, Zeng J-F, Jia Q-J, Du J, Shen L, Gao M-Y, Acta Physico-Chimica Sinica 2012, 28, 993.

[29]. Gao Z, Hou Y, Zeng J, Chen L, Liu C, Yang W, Gao M, Advanced Materials 2017, 29, 1701095.

[30]. Yuan Y, Ge SC, Sun HB, Dong XJ, Zhao HX, An LN, Zhang J, Wang JF, Hu B, Liang GL, Acs Nano 2015, 9, 5117. [PubMed: 25868488]

[31]. Tang XX, Gong XQ, Li A, Lin HY, Peng CY, Zhang XZ, Chen XY, Gao JH, Nano Letters 2020, 20, 363. [PubMed: 31838855]

[32]. Zheng MM, Wang YQ, Shi H, Hu YX, Feng LD, Luo ZL, Zhou M, He J, Zhou ZY, Zhang Y, Ye DJ, Acs Nano 2016, 10, 10075. [PubMed: 27934082]

[33]. Yu L, Chen Y, Wu M, Cai X, Yao H, Zhang L, Chen H, Shi J, Journal of the American Chemical Society 2016, 138, 9881. [PubMed: 27441571]

[34]. Khatik R, Wang ZY, Li FF, Zhi DB, Kiran S, Dwivedi P, Xu RX, Liang GL, Qiu BS, Yang Q, Nanomed-Nanotechnol 2019, 15, 264.

[35]. Wei J, Wang HM, Wu Q, Gong X, Ma K, Liu XQ, Wang F, Angewandte Chemie-International Edition 2019.

[36]. Gong F, Cheng L, Yang NL, Jin QT, Tian LL, Wang MY, Li YG, Liu Z, Nano Letters 2018, 18, 6037. [PubMed: 30141945]

[37]. Dong B, Song X, Kong X, Wang C, Tang Y, Liu Y, Lin W, Advanced Materials 2016, 28, 8755. [PubMed: 27545434]

[38]. Maeda H, Fukuyasu Y, Yoshida S, Fukuda M, Saeki K, Matsuno H, Yamauchi Y, Yoshida K, Hirata K, Miyamoto K, Angewandte Chemie International Edition 2004, 43, 2389. [PubMed: 15114569]

[39]. Zhang W, Liu W, Li P, Huang F, Wang H, Tang B, Analytical Chemistry 2015, 87, 9825. [PubMed: 26352695]

[40]. Abo M, Urano Y, Hanaoka K, Terai T, Komatsu T, Nagano T, Journal of the American Chemical Society 2011, 133, 10629. [PubMed: 21692459]

[41]. Xie X, Yang X. e., Wu T, Li Y, Li M, Tan Q, Wang X, Tang B, Analytical Chemistry 2016, 88, 8019. [PubMed: 27442152]

[42]. Gao W, Li X, Liu ZH, Fu W, Sun YH, Cao WH, Tong LL, Tang B, Analytical Chemistry 2019, 91, 1150. [PubMed: 30497260]

[43]. Ai XZ, Wang ZM, Cheong HL, Wang Y, Zhang RC, Lin J, Zheng YJ, Gao MY, Xing BG, Nature Communications 2019, 10.

[44]. Wang Z, Ai X, Zhang Z, Wang Y, Wu X, Haindl R, Yeow EKL, Drexler W, Gao M, Xing B, Chemical Science 2020, 11, 803.

[45]. Vaupel P, Kallinowski F, Okunieff P, Cancer Research 1989, 49, 6449. [PubMed: 2684393]

[46]. Gatenby RA, Gillies RJ, Nature Reviews Cancer 2004, 4, 891. [PubMed: 15516961]

[47]. Steen K, Steen A, Reeh P, The Journal of Neuroscience 1995, 15, 3982. [PubMed: 7751959]

[48]. Kostikas K, Papatheodorou G, Ganas K, Psathakis K, Panagou P, Loukides S, Am. J. Respir. Crit. Care Med 2002, 165, 1364. [PubMed: 12016097]

[49]. Hoffman AS, Advanced Drug Delivery Reviews 2013, 65, 10. [PubMed: 23246762]

[50]. Mura S, Nicolas J, Couvreur P, Nature Materials 2013, 12, 991. [PubMed: 24150417]

[51]. Huang WC, Chen RH, Peng Y, Duan F, Huang YF, Guo WS, Chen XY, Nie LM, Acs Nano 2019, 13, 9561. [PubMed: 31361949]

[52]. Wang ZM, Upputuri PK, Zhen X, Zhang RC, Jiang YY, Ai XZ, Zhang ZJ, Hu M, Meng ZY, Lu YP, Zheng YJ, Pu KY, Pramanik M, Xing BG, Nano Research 2019, 12, 49.

[53]. Hu YB, Han T, Yan N, Liu JK, Liu XL, Wang WX, Lam JWY, Tang BZ, Advanced Functional Materials 2019, 29.

[54]. Ding CP, Cheng SS, Zhang CL, Xiong YR, Ye MQ, Xian YZ, Analytical Chemistry 2019, 91, 7181. [PubMed: 31067856]

[55]. Zhang L, Yin TH, Li B, Zheng RQ, Qiu C, Lam KS, Zhang Q, Shuai XT, Acs Nano 2018, 12, 3449. [PubMed: 29634240]

[56]. Huang G, Zhao T, Wang C, Nham K, Xiong Y, Gao X, Wang Y, Hao G, Ge W-P, Sun X, Sumer BD, Gao J, Nature Biomedical Engineering 2020, 4, 314.

[57]. Yang GB, Xu LG, Chao Y, Xu J, Sun XQ, Wu YF, Peng R, Liu Z, Nature Communications 2017, 8.

[58]. Feng LL, Xie R, Wang CQ, Gai SL, He F, Yang D, Yang PP, Lin J, Acs Nano 2018, 12, 11000. [PubMed: 30339353]

[59]. Zhang PS, Hou Y, Zeng JF, Li YY, Wang ZH, Zhu R, Ma TC, Gao MY, Angewandte Chemie-International Edition 2019, 58, 11088. [PubMed: 31131511]

[60]. Li FY, Liang ZY, Liu JN, Sun JH, Hu X, Zhao M, Liu JX, Bai RL, Kim D, Sun XL, Hyeon T, Ling DS, Nano Letters 2019, 19, 4213. [PubMed: 30719918]

[61]. Yi ZG, Luo ZC, Barth ND, Meng XF, Liu H, Bu WB, All A, Vendrell M, Liu XG, Advanced Materials 2019, 31.

[62]. Wang S, Zhou ZJ, Wang ZT, Liu YJ, Jacobson O, Shen ZY, Fu X, Chen ZY, Chen X, Small 2019, 15.

[63]. Wang ZY, Ju YM, Ali Z, Yin H, Sheng FG, Lin J, Wang BD, Hou YL, Nature Communications 2019, 10.

[64]. Deryugina EI, Quigley JP, Cancer and Metastasis Reviews 2006, 25, 9. [PubMed: 16680569]

[65]. Yin L, Sun H, Zhang H, He L, Qiu L, Lin JG, Xia HW, Zhang YQ, Ji SJ, Shi HB, Gao MY, Journal of the American Chemical Society 2019, 141, 3265. [PubMed: 30689382]

[66]. Li XL, Bottini M, Zhang LY, Zhang S, Chen J, Zhang TB, Liu L, Rosato N, Ma XB, Shi XH, Wu Y, Guo WS, Liang XJ, Acs Nano 2019, 13, 176. [PubMed: 30592401]

[67]. Yang KK, Liu YJ, Wang Y, Ren QL, Guo HY, Matson JB, Chen XY, Nie ZH, Biomaterials 2019, 223.

[68]. Bassi DE, Lopez De Cicco R, Mahloogi H, Zucker S, Thomas G, Klein-Szanto AJP, Proceedings of the National Academy of Sciences 2001, 98, 10326.

[69]. Wang HY, Chen PY, Wu H, Zou P, Wu J, Liu YL, Liang GL, Analytical Chemistry 2019, 91, 14842. [PubMed: 31718142]

[70]. Yuan Y, Zhang J, Qi XL, Li SG, Liu GS, Siddhanta S, Barman I, Song XL, McMahon MT, Bulte JWM, Nature Materials 2019, 18, 1376. [PubMed: 31636420]

[71]. Vadas P, Browning J, Edelson J, Pruzanski W, J Lipid Mediat 1993, 8, 1. [PubMed: 8257775]

[72]. Yan RQ, Hu YX, Liu F, Wei SX, Fang DQ, Shuhendler AJ, Liu H, Chen HY, Ye DJ, Journal of the American Chemical Society 2019, 141, 10331. [PubMed: 31244188]

[73]. Wu CF, Zhang R, Du W, Cheng L, Liang GL, Nano Letters 2018, 18, 7749. [PubMed: 30481463]

[74]. Brentnall M, Rodriguez-Menocal L, De Guevara RL, Cepero E, Boise LH, BMC Cell Biology 2013, 14, 32. [PubMed: 23834359]

[75]. Porter AG, Jänicke RU, Cell Death & Differentiation 1999, 6, 99. [PubMed: 10200555]

[76]. Akazawa K, Sugihara F, Nakamura T, Mizukami S, Kikuchi K, Bioconjugate Chemistry 2018, 29, 1720. [PubMed: 29714062]

[77]. Zheng FF, Wang C, Meng TT, Zhang YQ, Zhang PH, Shen Q, Zhang YC, Zhang JF, Li JX, Min QH, Chen JN, Zhu JJ, Acs Nano 2019, 13, 12577. [PubMed: 31657911]

[78]. Chen Z, Chen M, Cheng Y, Kowada T, Xie J, Zheng X, Rao J, Angew Chem Int Ed Engl 2020, 59, 3272. [PubMed: 31828913]

[79]. Harris AL, Nature Reviews Cancer 2002, 2, 38. [PubMed: 11902584]

[80]. Vannucci SJ, Hagberg H, Journal of Experimental Biology 2004, 207, 3149.

[81]. Konisti S, Kiriakidis S, Paleolog EM, Nature Reviews Rheumatology 2012, 8, 153. [PubMed: 22293762]

[82]. Bertout JA, Patel SA, Simon MC, Nature Reviews Cancer 2008, 8, 967. [PubMed: 18987634]

[83]. Semenza GL, Journal of Applied Physiology 2000, 88, 1474. [PubMed: 10749844]

[84]. Ke Q, Costa M, Molecular Pharmacology 2006, 70, 1469. [PubMed: 16887934]

[85]. Fan YS, Lu M, Yu XA, He ML, Zhang Y, Ma XN, Kou JP, Yu BY, Tian JW, Analytical Chemistry 2019, 91, 6585. [PubMed: 30994329]

[86]. Qin XJ, Si YM, Wang DW, Wu ZY, Li JS, Yin YD, Analytical Chemistry 2019, 91, 4529. [PubMed: 30830752]

[87]. Li YT, Liu JM, Wang ZC, Jin J, Liu YL, Chen CY, Tang ZY, Advanced Materials 2020.

[88]. Zheng X, Cui L, Chen M, Soto LA, Graves EE, Rao J, Cancer Research 2019, 79, 4787. [PubMed: 31311808]

[89]. Xu G, Yan Q, Lv X, Zhu Y, Xin K, Shi B, Wang R, Chen J, Gao W, Shi P, Fan C, Zhao C, Tian H, Angewandte Chemie International Edition 2018, 57, 3626. [PubMed: 29393566]

[90]. Shi B, Ren N, Gu L, Xu G, Wang R, Zhu T, Zhu Y, Fan C, Zhao C, Tian H, Angewandte Chemie International Edition 2019, 58, 16826. [PubMed: 31532051]

[91]. Wu L, Sun Y, Sugimoto K, Luo Z, Ishigaki Y, Pu K, Suzuki T, Chen H-Y, Ye D, Journal of the American Chemical Society 2018, 140, 16340. [PubMed: 30384600]

[92]. Wu L, Ishigaki Y, Hu Y, Sugimoto K, Zeng W, Harimoto T, Sun Y, He J, Suzuki T, Jiang X, Chen H-Y, Ye D, Nature Communications 2020, 11, 446.

[93]. Knowles JR, Annual Review of Biochemistry 1980, 49, 877.

[94]. Pellegatti P, Raffaghello L, Bianchi G, Piccardi F, Pistoia V, Di Virgilio F, PLOS ONE 2008, 3, e2599. [PubMed: 18612415]

[95]. Di Virgilio F, Sarti AC, Falzoni S, De Marchi E, Adinolfi E, Nature Reviews Cancer 2018, 18, 601. [PubMed: 30006588]

[96]. Zhou Y, Tozzi F, Chen J, Fan F, Xia L, Wang J, Gao G, Zhang A, Xia X, Brasher H, Widger W, Ellis LM, Weihua Z, Cancer Research 2012, 72, 304. [PubMed: 22084398]

[97]. Zhao J, Gao JH, Xue WT, Di ZH, Xing H, Lu Y, Li LL, Journal of the American Chemical Society 2018, 140, 578. [PubMed: 29281270]

[98]. Di Z, Zhao J, Chu H, Xue W, Zhao Y, Li L, Advanced Materials 2019, 31, 1901885.

[99]. Liu B, Ma R, Zhao J, Zhao Y, Li L, Science China Chemistry 2020, 63, 1490.

[100]. Song XR, Li SH, Guo HH, You WW, Tu DT, Li J, Lu CH, Yang HH, Chen XY, Advanced Science 2018, 5.

[101]. Cairns RA, Harris IS, Mak TW, Nature Reviews Cancer 2011, 11, 85. [PubMed: 21258394]

[102]. Yu J, Zhao F, Gao WL, Yang X, Ju YM, Zhao LY, Guo WS, Xie J, Liang XJ, Tao XY, Li J, Ying Y, Li WC, Zheng JW, Qiao L, Xiong SB, Mou XZ, Che SL, Hou YL, Acs Nano 2019, 13, 10002. [PubMed: 31433945]

[103]. Luo Y, Kim EH, Flask CA, Clark HA, Acs Nano 2018, 12, 5761. [PubMed: 29851460]

[104]. Zhao Y, Shi C, Yang XD, Shen BW, Sun YQ, Chen Y, Xu XW, Sun HC, Yu K, Yang B, Lin Q, Acs Nano 2016, 10, 5856. [PubMed: 27232534]

[105]. Teng LL, Song GS, Liu YC, Han XY, Li Z, Wang YJ, Huan S, Zhang XB, Tan WH, Journal of the American Chemical Society 2019, 141, 13572. [PubMed: 31370392]

[106]. Zheng X, Mao H, Huo D, Wu W, Liu B, Jiang X, Nature Biomedical Engineering 2017, 1, 0057.

[107]. Zheng JD, Wu YX, Xing D, Zhang T, Nano Research 2019, 12, 931.

[108]. Hou Y, Zhou J, Gao Z, Sun X, Liu C, Shangguan D, Yang W, Gao M, ACS Nano 2015, 9, 3199. [PubMed: 25670342]

[109]. Ma TC, Hou Y, Zeng JF, Liu CY, Zhang PS, Jing LH, Shangguan D, Gao MY, Journal of the American Chemical Society 2018, 140, 211. [PubMed: 29237264]

[110]. Stack J, Redmond O, Codd M, Dervan P, Ennis J, Radiology 1990, 174, 491. [PubMed: 2296657]

[111]. Hueftle M, Modic M, Ross J, Masaryk T, Carter J, Wilber R, Bohlman H, Steinberg P, Delamarter R, Radiology 1988, 167, 817. [PubMed: 2966418]

[112]. Brant-Zawadzki M, Berry I, Osaki L, Brasch R, Murovic J, Norman D, American Journal of Roentgenology 1986, 147, 1223. [PubMed: 3490758]

[113]. Sadowski EA, Bennett LK, Chan MR, Wentland AL, Garrett AL, Garrett RW, Djamali A, Radiology 2007, 243, 148. [PubMed: 17267695]

[114]. FDA, Vol. 2020, U. S. Food & Drug Administration, 2018.

[115]. Hansen AE, Petersen AL, Henriksen JR, Boerresen B, Rasmussen P, Elema DR, Rosenschöld P. M. a., Kristensen AT, Kjær A, Andresen TL, ACS Nano 2015, 9, 6985. [PubMed: 26022907]

[116]. Sindhwani S, Syed AM, Ngai J, Kingston BR, Maiorino L, Rothschild J, MacMillan P, Zhang Y, Rajesh NU, Hoang T, Wu JLY, Wilhelm S, Zilman A, Gadde S, Sulaiman A, Ouyang B, Lin Z, Wang L, Egeblad M, Chan WCW, Nature Materials 2020, 19, 566. [PubMed: 31932672]

[117]. Nel AE, Mädler L, Velegol D, Xia T, Hoek EMV, Somasundaran P, Klaessig F, Castranova V, Thompson M, Nature Materials 2009, 8, 543. [PubMed: 19525947]

[118]. Zhang Z, Guan J, Jiang Z, Yang Y, Liu J, Hua W, Mao Y, Li C, Lu W, Qian J, Zhan C, Nature Communications 2019, 10, 3561.

[119]. Park J-H, Gu L, Von Maltzahn G, Ruoslahti E, Bhatia SN, Sailor MJ, Nature materials 2009, 8, 331. [PubMed: 19234444]

[120]. Yu M, Zheng J, ACS nano 2015, 9, 6655. [PubMed: 26149184]

[121]. Liu J, Yu M, Zhou C, Yang S, Ning X, Zheng J, Journal of the American Chemical Society 2013, 135, 4978. [PubMed: 23506476]

[122]. Song G, Hao J, Liang C, Liu T, Gao M, Cheng L, Hu J, Liu Z, Angewandte Chemie International Edition 2016, 55, 2122. [PubMed: 26710169]

[123]. Du BJ, Jiang XY, Das A, Zhou QH, Yu MX, Jin RC, Zheng J, Nature Nanotechnology 2017, 12, 1096.

[124]. Sun XR, Wang GW, Zhang H, Hu SQ, Liu X, Tang JB, Shen YQ, Acs Nano 2018, 12, 6179. [PubMed: 29847730]

[125]. Ma M, Zhu H, Ling J, Gong S, Zhang Y, Xia Y, Tang Z, ACS Nano 2020, 14, 4036. [PubMed: 32196312]

[126]. Mirshafiee V, Sun B, Chang CH, Liao Y-P, Jiang W, Jiang J, Liu X, Wang X, Xia T, Nel AE, ACS Nano 2018, 12, 3836. [PubMed: 29543433]

[127]. Meng H, Xia T, George S, Nel AE, ACS Nano 2009, 3, 1620. [PubMed: 21452863]

[128]. Wang X, Chang CH, Jiang J, Liu X, Li J, Liu Q, Liao Y-P, Li L, Nel AE, Xia T, Small 2020, 16, 2000528.

[129]. Wang X, Lee J-H, Li R, Liao Y-P, Kang J, Chang CH, Guiney LM, Mirshafiee V, Li L, Lu J, Xia T, Hersam MC, Nel AE, Small 2018, 14, 1703915.

[130]. Nel A, Xia T, Meng H, Wang X, Lin S, Ji Z, Zhang H, Accounts of Chemical Research 2013, 46, 607. [PubMed: 22676423]

[131]. Liu Q, Wang X, Xia T, Analytical and Bioanalytical Chemistry 2018, 410, 6097. [PubMed: 30066194]

[132]. George S, Xia T, Rallo R, Zhao Y, Ji Z, Lin S, Wang X, Zhang H, France B, Schoenfeld D, Damoiseaux R, Liu R, Lin S, Bradley KA, Cohen Y, Nel AE, ACS Nano 2011, 5, 1805. [PubMed: 21323332]

[133]. Wang X, Liao Y-P, Telesca D, Chang CH, Xia T, Nel AE, Small 2017, 13, 1700776.

[134]. Wang X, Sun B, Liu S, Xia T, NanoImpact 2017, 6, 99. [PubMed: 28480337]

[135]. Mirshafiee V, Jiang W, Sun B, Wang X, Xia T, Molecular Therapy 2017, 25, 1522. [PubMed: 28412168]

[136]. Hwang R, Mirshafiee V, Zhu Y, Xia T, Ecotoxicology and Environmental Safety 2018, 166, 294. [PubMed: 30273853]

[137]. Lin S-J, Guarente L, Current Opinion in Cell Biology 2003, 15, 241. [PubMed: 12648681]

[138]. Chen ZX, Chen M, Cheng YF, Kowada T, Xie JH, Zheng XC, Rao JH, Angewandte Chemie-International Edition 2019.

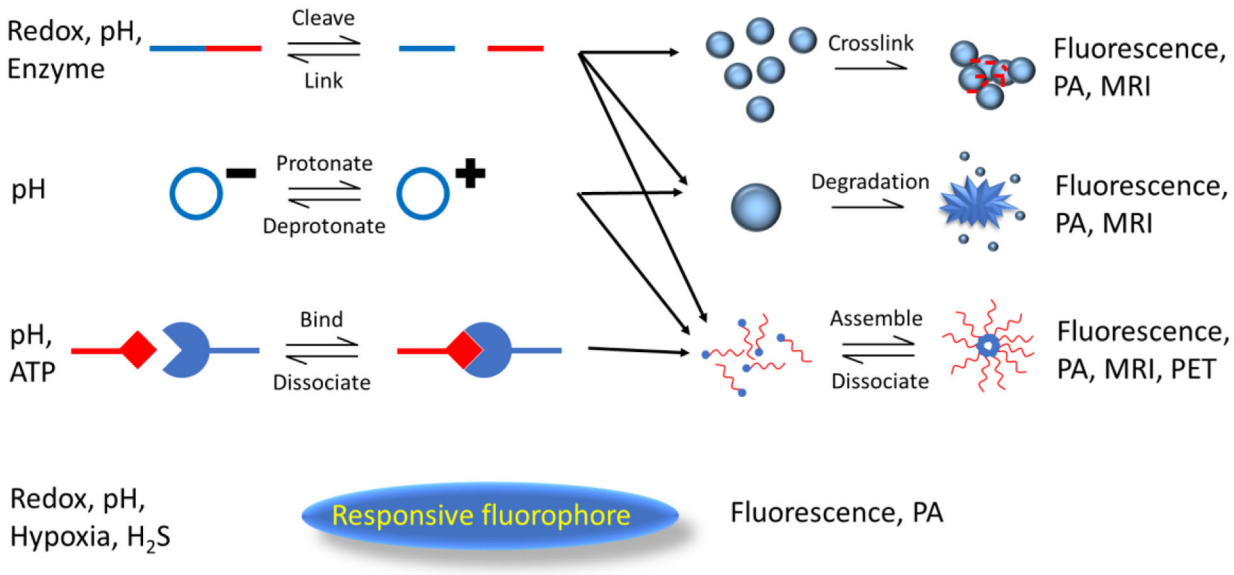

Figure 1.
The illustration of activatable nanoprobes for bioimaging in this review.

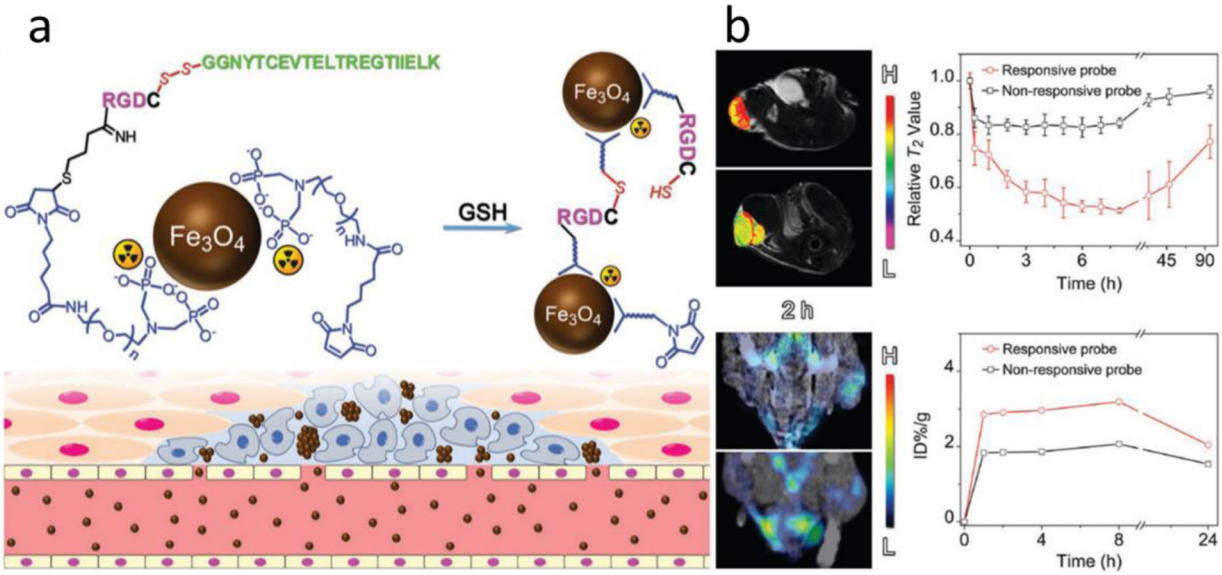

Figure 2.

a) Illustration to demonstrate the aggregation of ^{99m}Tc-labeled Fe_3O_4 nanoparticles in the tumor microenvironment through GSH induced interparticle crosslinking reaction. b) T2-weighted MR images of tumor-bearing mice acquired 2 h after the intravenous injections of the responsive probe (top left) and the nonresponsive probes (bottom left), together with T2 values extracted from the tumor sites before and at different time points after the intravenous injections (right). b) SPECT/CT images of tumor-bearing mice acquired 2 h after the intravenous injections with the responsive probe (top left) and the control probe (bottom left), respectively, together with temporal γ-signals of the tumorous areas (right). Reproduced with permission.[29] Copyright 2017 WILEY-VCH Verlag GmbH & Co. KGaA, Weinheim

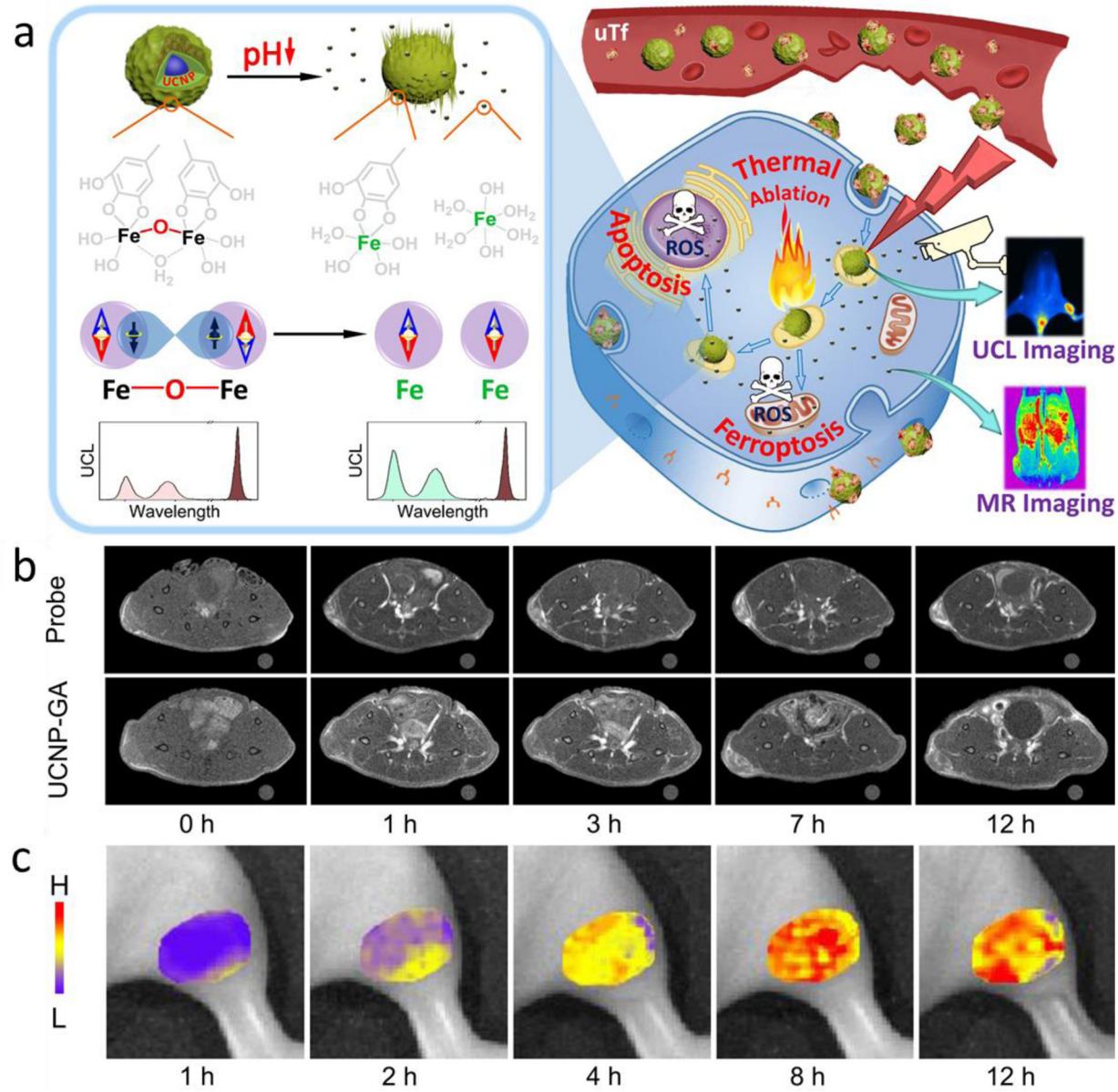

Figure 3.

a) Illustration to demonstrate the activatable probe for MRI and its therapeutic function. The probe accumulates in the tumor through the impaired blood vessel after intravenous injection. Transferrin receptor-induced tumor ingestion of probes. Low pH could activate the probe and release FeIII, enhancing the T1 imaging. Released FeIII accelerates tumor cell death through upregulated ROS, while the remained GA-FeIII irradiation for PTT. b) T1-weighted MR images of tumor-bearing mice acquired at different time points pre- and post-injection of the probe and UCNP-GA control, respectively. c) The upconversion luminescence imaging based on the I_{475}/I_{800} ratio revealed the release of Fe^{3+} ions. Reproduced with permission.[59] Copyright 2019 Wiley-VCH Verlag GmbH & Co. KGaA, Weinheim.

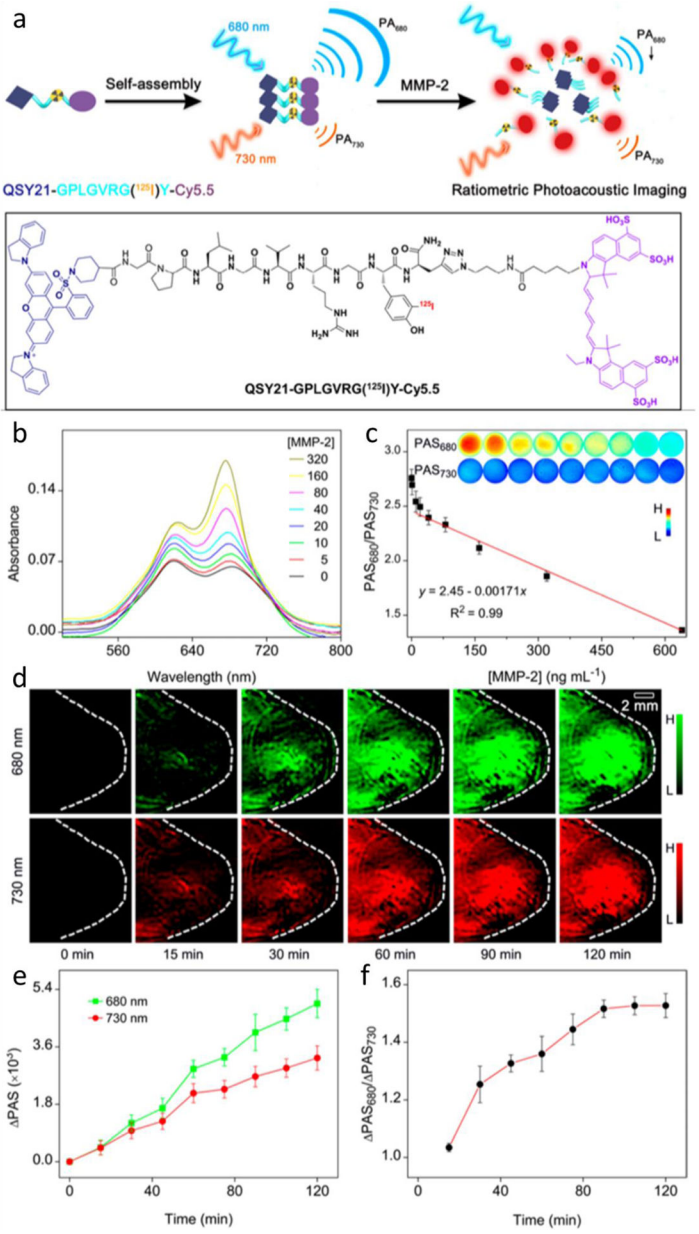

Figure 4.

a) Scheme and structure of a non-invasively fluorescence/photoacoustic probe for MMP-2 activity imaging. b) The UV-vis absorption spectra of the probe (8 μM) after incubation in different MMP-2 concentrations (ng mL^{-1}). c) After incubation in different MMP-2 concentrations for 2 h, the ratio of ΔPAS680/ ΔPAS730 (0.25 μM) and the concentration of MMP2 recorded at 37 °C (inset: PA images of the probe solutions under different amounts of MMP-2). d) The PA images of tumor-bearing mice acquired after injection with the probe (60 μM, 200 μL) at different time points under the illumination of 680 and 730 nm, respectively. The tumor regions are delineated by white dotted circles. e) Temporal PA signal (ΔPAS) of the tumor site after subtracting the pre-contrasted signal recorded under

illumination at 680 and 730 nm, respectively. f) Temporal ratiometric signal ΔPAS680/ΔPAS730 at different time points after injection of the probe.
Reproduced with permission.[65] Copyright 2019, American Chemical Society

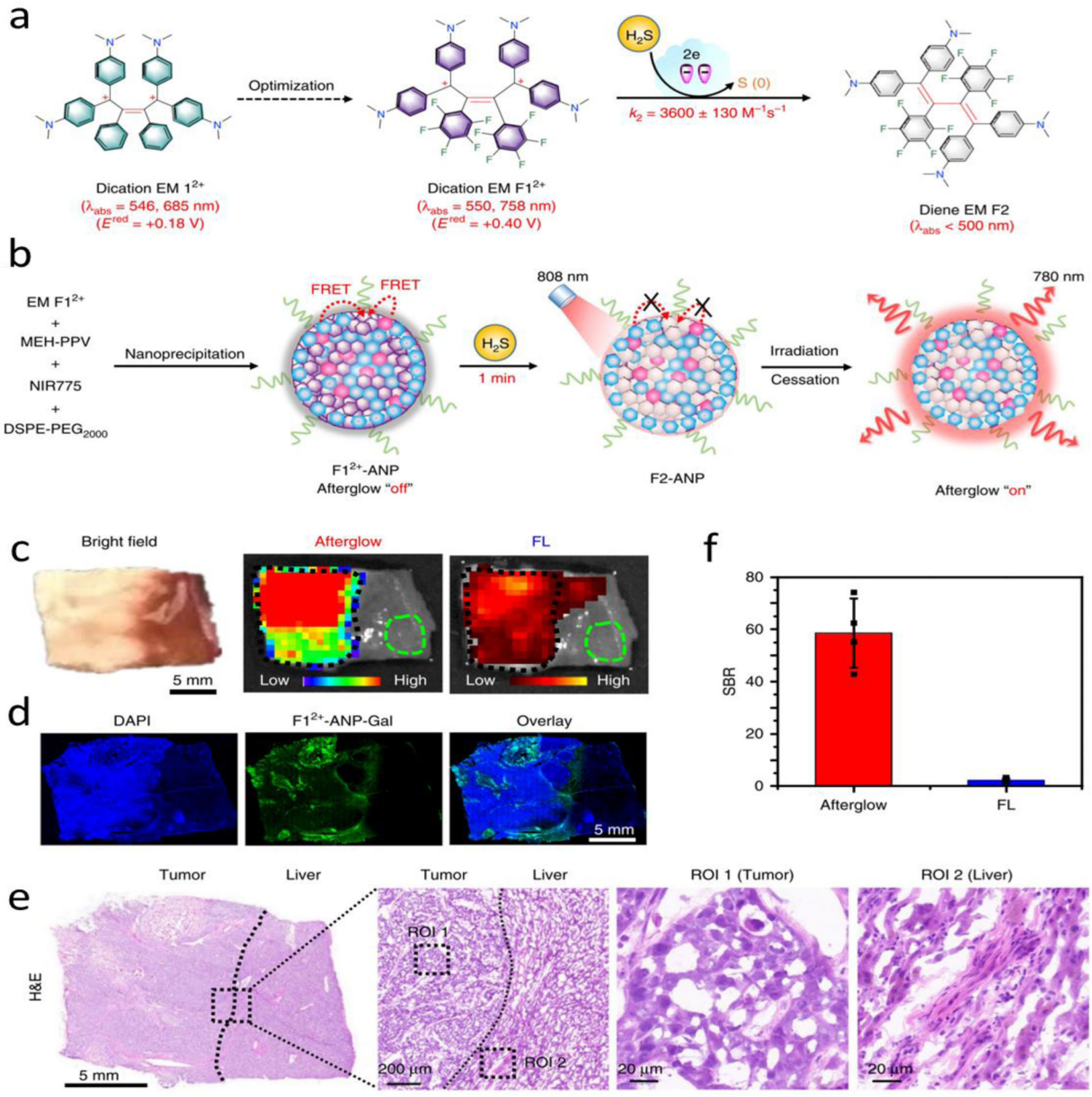

Figure 5.

a) By introducing two electron-withdrawing pentafluorophenyl groups, the EM 1^{2+} was optimized into EM $F1^{2+}$, which can be reduced by H_2S into EM F2. b) Scheme of the Preparation and H_2S induced NIR afterglow of $F1^{2+}$-ANP. c) The photograph (bright field), afterglow, and FL images of the liver specimen resected from an HCC patient. The specimen was incubated with $F1^{2+}$-ANP-Gal in PBS buffer (1×, pH 7.4) at 37 °C for 3 h, and then washed three times with PBS buffer. After irradiated with the 808-nm laser (1Wcm^{-2}, 1 min), the afterglow image was acquired under an open filter (exposure: 60 s). The fluorescence image was collected with λex/em =740/790 nm. d) The fluorescence imaging of liver tissue slices from c), which was incubated with $F1^{2+}$-ANP-Gal (green) for 3 h and stained with DAPI (blue). e) H&E staining of the liver tissue slice. Black dash boxes indicate the enlarged areas, in which box ROI 1 shows the tumor tissue, and box ROI 2

indicates the normal liver tissue, respectively. f) Quantitative analysis of the average SBRs for afterglow and fluorescence imaging of liver specimens resected from HCC patients. Data denote mean ± sd. (n = 4).

Reproduced with permission.[92] Copyright 2020, Springer Nature.

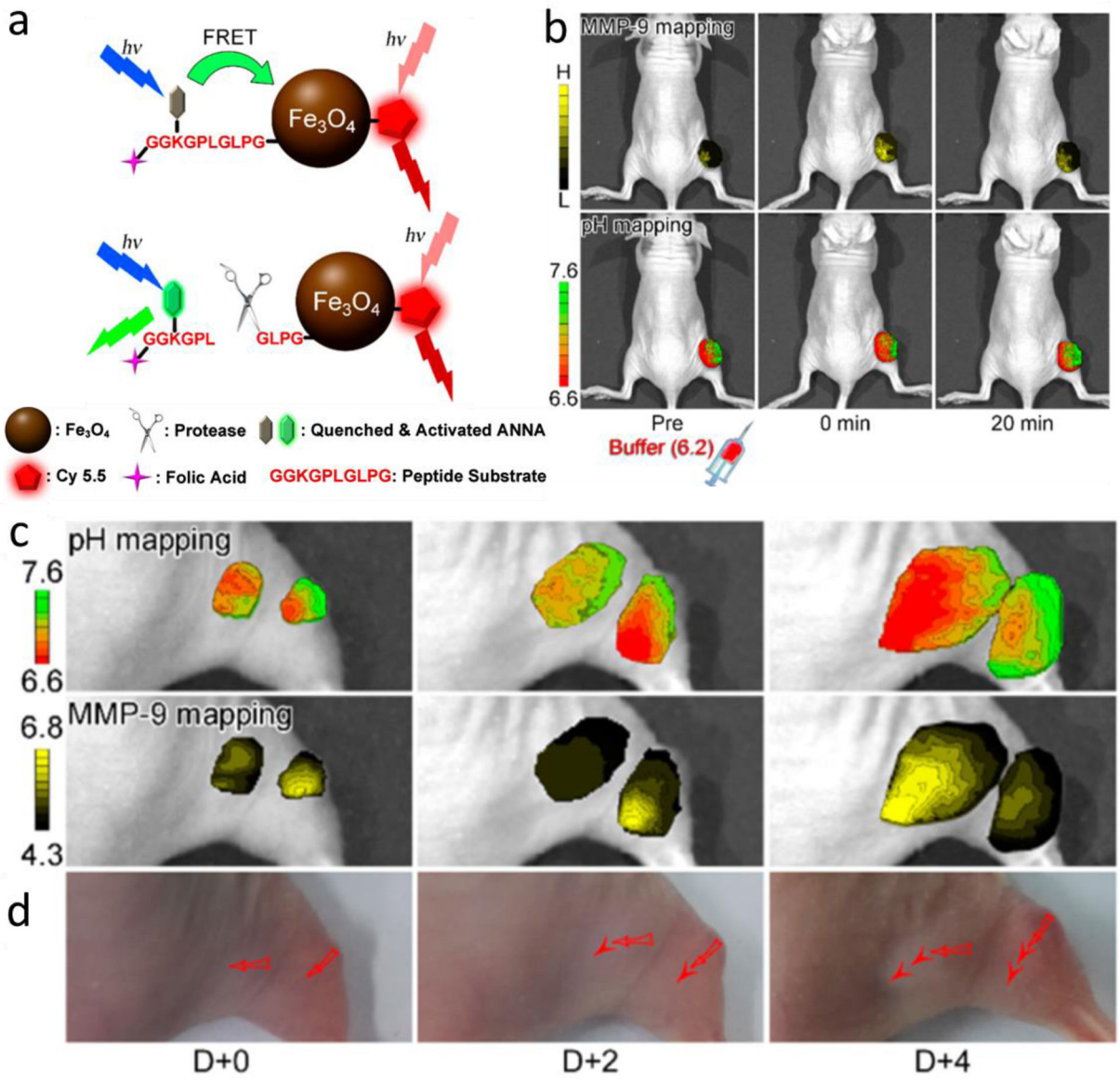

Figure 6.

a) Scheme of the nanoprobe. Upon cleavage of the peptide linker, the fluorescence of ANNA would be activated. Cy5.5 is always in an “on” state. Folic acid was modified to enhance tumor target ability. b) Mapping of MMP-9 activity after intratumoral injection of low pH PBS (pH 6.2). c) Quantified pH and MMP-9 expression mapping of tumors obtained at D+0 day, D+2, and D+4 (in color bar shading from black to yellow for reading MMP-9 expression ranging from 4.3−6.8 ng/mL; each step thus corresponds to 0.25 units). d) Photographs of tumors showing their growth in four days.

Reproduced with permission.[109] Copyright 2018, American Chemical Society

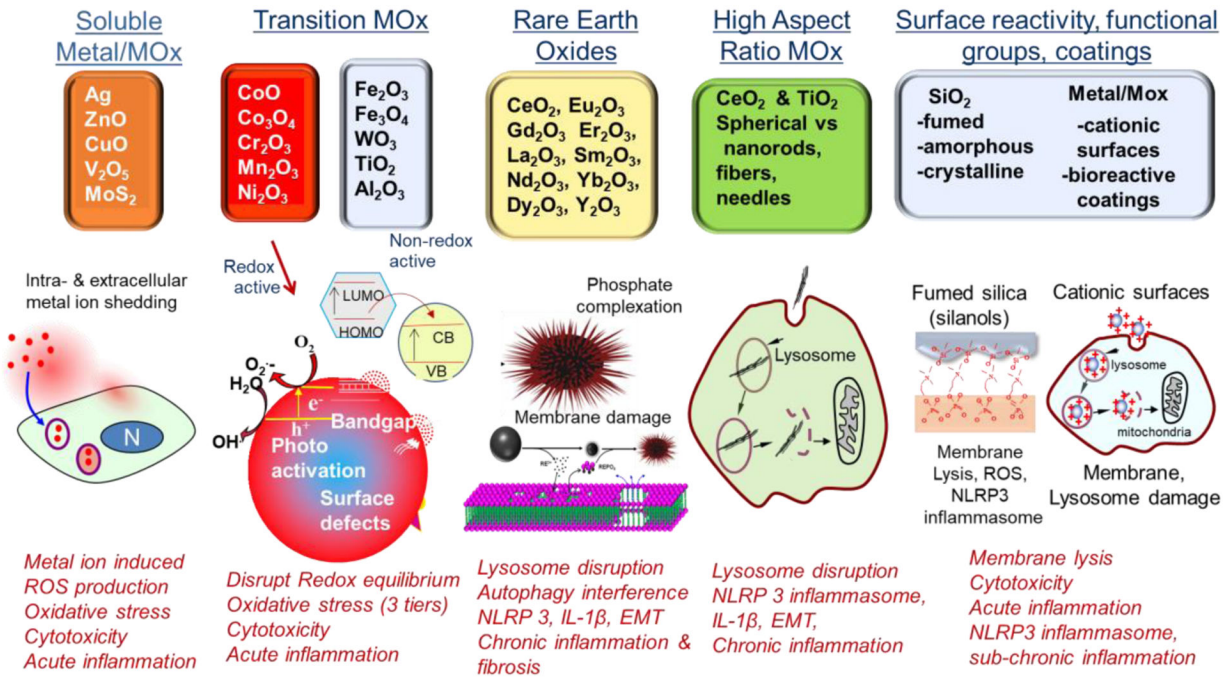

Figure 7.

Schematic showing the mechanisms of metals and metal oxide nanoparticle toxicity, as determined by the toxicological profiling of dozens of these materials in macrophages and the intact lung. Soluble MOxs and redox-active TMOs induce ROS production and oxidative stress due to the release of toxic metal ions and overlap of conduction band energy with the cellular redox potential, respectively. In contrast, the lysosomal dissolution of REOs in an acidic environment, except for CeO2 nanoparticles, leads to the release of rare-earth ions that, upon complexation to biological phosphates precipitate on the particle surface, leading to biotransformation into urchin-shaped structures. This triggers lysosomal damage, NLRP3 inflammasome activation, and IL-1β production. High aspect ratio materials trigger lysosomal damage and NLRP3 inflammasome activation. Fumed silica induces membrane lysis, potassium efflux, and NLRP3 inflammasome activation. Cationic nanoparticles induce lysosomal damage and cell death.

Table 1.

Redox responsive nanoprobes for *in vivo* imaging.

Imaging model	Nanoprobe	Stimuli	Response mechanism	Route and dose	Tissue or organ	Dynamics	Ref
Fluorescence	Au/Pt star@S-S@rHSA-FA@IR780@GOx	GSH	Disulfide linker was cleaved by GSH	Intravenously injection 5 mg/kg (IR780)	Tumor	Accumulated in the tumor tissue with prolonged circulation time from 2 to 36 h, and still displayed remarkable signal after 48 h post-injection.	[25]
	Nanomicelle			Intravenously injection 200 μL (0.1 mg/mL)	Tumor	Faint fluorescence in tumors could be observed at 6 h post-injection. The fluorescence intensity gradually enhanced, reaching the maximum intensity at 12 h post-injection and maintained for a long period.	[26]
	GSH modified, lanthanide-based nanoparticles	ROS	Crosslinking (The sulfhydryl group was oxidized by ROS to form a disulfide bond)	Intravenously injection 5 mg/kg	Inflamed epidermal area	Bright NIR-II signal at the inflamed epidermal area was observed after 10 minutes and remained stable for 8 hours.	[27]
T2 MRI/SPECT	^{99m}Tc-Labeled Fe_3O_4 Nanoprobes	GSH	Crosslinking (Upon cleavage of the disulfide bond by GSH, the thiol group will react with the remaining maleimide residues from adjacent particles.	Intravenously injection 10 mg/kg (Fe^{3+})	Tumor	blood residence time: 8.2 h for the nonresponsive probe and 6.4 h for the responsive probe.	[29]
^{19}F MRI	oligomer self-assembled nanoparticle	GSH/ Legumain	GSH-controlled assemble and the legumain-controlled disassemble	Enterocoelia injection 1.5 g/kg	Tumor	Two hours after the injection, strong signals were observed from the tumor.	[30]
	Polymers and ICG self-assembled nanoparticle	GSH	Disulfide linker was cleaved by GSH	Subcutaneous injection, intratumoral injection, intravenously injection 100–200 μL (7 mM)	Tumor	A clear fluorescence signal in the tumor was observed at 1 h after injection.	[31]
Fluorescence/^{19}F-MRS/^{1}H-MRI	self-assembled nanoparticle	GSH	Disulfide linker was cleaved by GSH	Intravenously injection 0.025 mmol/kg	Tumor, liver	The maximum fluorescence and ^{1}H-MRI were achieved by 60 min,	[32]
T1/T2 MRI	Janus NPs (Fe_3O_4 & SiO_2)	GSH	GSH induced Mn^{2+} release	Intravenously injection 2.5 mg/kg (Fe)	Tumor, liver	A significantly brighter signal was observed at 60 min post-injection	[34]
Fluorescence/MRI	honeycomb MnO_2 nanosponge-sustained autocatalytic DNAzyme	GSH	GSH induced Mn^{2+} release	Intravenously injection 3.5 mg/kg (Fe)	Tumor	The signal presented an increasing trend with extended duration and reached the maximum value after 6 h of injection	[35]
PA/T1 MRI	MnMoOX-PEG	GSH	Reduction of Mo^{VI} in the initial MnMoOx to Mo^{V} by GSH	Intratumoral injection, intravenously injection 20 mg/kg	Tumor	An obvious brightening effect could be observed in the tumor region after injection at 4–24 h	[36]

Imaging model	Nanoprobe	Stimuli	Response mechanism	Route and dose	Tissue or organ	Dynamics	Ref
PA	Self-assembled BSA-Cy-Mito nanoprobe	GSH/H_2O_2	Redox dependent fluorophores	Intravenously injection 10 mg/kg	Abdominal aortas	PA imaging was conducted 2 h post-injection.	[42]
PA (MSOT) / Fluorescence	photon-upconverting nanoprobe	ROS/RNS	Redox dependent fluorophores	Intravenously injection 100 μL (5 mg/mL)	Liver	Response was easily observed within 3 h	[43]
		H_2O_2				Ratiometric imaging indicates the oxidative burst induced by INH within 30 min	[44]

Table 2.

pH responsive nanoprobes for *in vivo* imaging.

Imaging model	Nanoprobe	Stimuli	Response mechanism	Route and dose	Tissue or organ	Dynamics	Ref
PA	polyaniline and Au triangular nanoplates	pH 1–8	PANI has protonated transits from blue to green (reversible).	Oral administration 200 μL (30 μg/mL)	Gastric and Intestinal function	PA signal was soon observed in the stomach about 20 min later	[51]
	self-assembled 3,3',5,5'-tetramethylbenzidine	pH 5–9	Low pH results in the color change and degradation of charge-transfer nanocomplex.	Intratumorally injection 200 μL (1 mg/mL)	Tumor	At 4 h post-injection, the difference of PA intensity was observed between tumor and normal tissue.	[52]
Fluorescence	oxazine-containing polyheterocycles	ammonia (pH 1–9)	the protonation and deprotonation processes occurred on the imine nitrogen (C=N)	Incubate in culture medium 10×10^{-6} M	Intestine	Fluorescent images were taken after incubation for 4 h.	[53]
	UCNPs@SiO2-Ag_2S	pH 4–9	dissociation of −COOH and the deprotonation of −NH2 groups on the surface of the Ag_2S prolong the fluorescence lifetime, improve fluorescence emission efficiency, and enhance the fluorescence intensity	Microinjected into the yolk sac 4.0 μg	Tumor	The difference can be observed at 0.5 h	[54]
US	polymersome-based, perfluorocarbon encapsulated nanoprobe	pH 6.8–7.4	The protonation of copolymer increases the size of the nanoprobe	Intravenously injection 4 mg/kg	Tumor	Post-injection time points, 5, 11, and 24 h, representing weak, strong, and persistent tumor Accumulation.	[55]
PET	^{64}Cu-labeled polymers	pH 6.5–7.4	Lowering the pH below the transition pH (6.9) led to micelle dissociation into unimers (8.4 ± 0.2 nm)	Intravenously injection 150 μL (100 μCi)	Tumor	The tissue uptake were 9.9±2.5, 6.5±2.5, and 5.7±1.2 %ID/g in the HN5, FaDu, and 4T1 tumors 18–24 h after injection	[56]
T1 MRI/ Fluorescence	Hollow MnO2-PEG/C&D	pH 6.0–7.4	The decomposition of MnO_2 into Mn^{2+} ions in an acid condition.	Intravenously injection 10 mg/kg (MnO_2)	Tumor	The fluorescence signals in the tumor region increased and reached a peak level at 8 h post-injection. At 24 h post-injection, the T1-MR signals showed twofold-positive enhancement in the tumor.	[57]
T1/T2 MRI	Fe_5C_2-GOD@MnO_2	pH 6.0–7.4	Decomposition of MnO_2 shell in an acid environment.	Intravenously injection 10 mg/kg (Fe)	Tumor	The half-time (τ1/2) was calculated to be ~3.23 h.	[58]
T1 MRI/ Fluorescence	UCNP@GA-Fe^{III}	pH 3.0–8.0	Unsaturated coordination Fe^{III} release in an acid condition.	Intravenously injection 15 mg/kg (Gd)	Tumor	T1 is shortened straightforwardly by 49% at 7 h post-injection and further decreased by 54% at 24 h. Fluorescence signal appears at the tumor site 2 h post-injection.	[59]
T1 MRI	Iron Oxide Nanoparticle Assemblies	pH 5.5–7.4	Disassembly due to the cleavage of hydrazone linkage (−C=N−N−) in an acid environment	Intravenously injection 4 mg/kg (Fe)	Tumor	Blood circulation half-life time of ~2.2 h	[60]

Imaging model	Nanoprobe	Stimuli	Response mechanism	Route and dose	Tissue or organ	Dynamics	Ref
	$NaGdF_4$-$CaCO_3$ Nanoconjugates	pH 5.0–7.4	Acid induced disintegration of the $CaCO_3$ lead to the exposure of $NaGdF_4$.	Intravenously injection 2.5 μmol (Gd)	Tumor	The tumor site started lighting up ≈30 min post-injection.	[61]
	Gadolinium metallofullerene encapsulated in polymer nanoparticles	pH 6.6–7.4	The protonation of poly (2-(diisopropylamino)ethyl methacrylate)-(2-(diethylamino)ethyl methacrylate) segments lead to the dissociation of nanoparticles	Intravenously injection 150 μL, (0.5×10^{-3} M Gd)	Tumor	At 24 h post-injection, the tumor uptake efficiency reached 4.79% ID/g.	[62]
T2 MRI/ Fluorescence	DOX-ICG @Fe/FeO-PPP-FA nanocapsules	pH 5.4–7.4	The instability of Fe/FeO nanocrystals in weak acidic condition	Intravenously injection 20 mg/kg	Tumor	Strong fluorescence and MR signals were still observed in the tumor site after 12 h.	[63]

Table 3.

Enzyme responsive nanoprobes for *in vivo* imaging.

Imaging model	Nanoprobe	Stimuli	Response mechanism	Route and dose	Tissue or organ	Dynamics	Ref
PA/ Fluorescence	ICG/DOX@Gel-CuS	Proteases	Upon the erosion of the gelatin matrix by protease, the DOX release and the fluorescence of ICG were recovered.	Intravenously injection 25 μL (2.75 mg/mL)	Tumor	Tumor-site accumulation efficiency: 7.02% ID/g and 5.66% ID/g at 4 and 24 h post-injection	[66]
PA	Au NPs	MMPs	The cleavage of MMP-cleavable peptide linker induced the aggregation of NPs	Intravenously injection 50 mg/kg	Tumor	Tumor uptake: 5.59 ± 0.52% ID/g (Imaging Analysis), 3.94 ± 2.01% ID/g (ICP-MS) at 24 h post-injection.	[67]
PET	Acetyl-Arg-Val-Arg-Arg-Cys(StBu)-Lys(DOTA-^{68}Ga)-CBT	Furin	After reduction and furin cleavage, the precursor is subjected to click condensation reaction to yield the cyclized oligomers, which self-assemble into Ga nanoparticles	Intravenously injection 20 mg/kg	Tumor	Tumors were visualized at 1 h post-injection. (2.6% ID/g)	[69]
MRI (CEST)	Olsa-RVRR		The peptide is cleaved by furin, initiating a click condensation reaction between the GSH-induced 1,2-aminothiol group (d-cysteine) and the cyano group of the CBT motif, initiating the formation of clusters of aggregated Olsa nanoparticles.	Intravenously injection 278 mg/kg	Tumor	The maximum Olsa CEST signal was observed at 2 h post-injection.	[70]
T1 MRI/ Fluorescence	P-CyFF-Gd	ALP	The probe is dephosphorylated by membrane-bound ALP and converted into fluorescent CyFF-Gd, which subsequently self-assembles into a fluorescent and magnetic NPs.	Intravenously injection 200 μL (50 μM)	Tumor	Tumor fluorescence peaked at 2 h post-injection. (23.5% ID/g) The maximum MR signal enhancement (%SE) in tumors was ~58% at 4 h post-injection.	[72]
PA	IR775-PhePhe-Tyr(H_2PO_3)-OH		Upon ALP dephosphorylation, self-assembles into nanostructures with enhanced PA signal.	Intratumorally injection 0.5 μmol/kg	Tumor	The maximal contrast ratio was reached at 4 h after injection.	[73]
^{19}F MRI	FLAME (liquid perfluorocarbon core and a robust silica shell) - DEVD ($Gd3^+$ complex-conjugated peptide)	Caspase-3/7	The peptides are cleaved by caspase-3, the Gd^{3+} complexes diffuse away from the FLAME surface, resulting in the recovery of the ^{19}F MRI signal.	Intravenously injection 200 μL (10 mM)	Apoptotic cell (Spleen and Liver)	^{19}F MRI images were acquired 24 h after injection.	[76]
Fluorescence	Cyt c-US@DS@HA	hyaluronidase	The digestion of outermost HA protective shell and the outer frame degradation, induced protein release and UCL restoration of UCNPs	Intravenously injection 100 μL (3 mg)	Tumor	Fluorescence accumulation was observed in the tumor site at 48 h post-injection	[77]
Fluorescence	The scaffolds made of 2-pyrimidinecarbonitrile and cysteine joined by a benzyl linker	Protease and Glycosidase	The condensation reaction between aromatic nitrile and aminothiol units promotes nano-assembly	Incubation 20 μL	-	-	[138]

Table 4.

The intravenous nanoparticles for imaging that are currently undergoing clinical trials.

Imaging model	Nanoparticle	Conditions	Phases	NCT Number	Status
MRI/US	AuroShells®	Neoplasms of the Prostate	Not applicable	NCT04240639 NCT02680535	Recruiting
MRI	USPIO	Coronary Artery Disease		NCT03451448	Recruiting
MRI	SPIO	Myocardial Infarction Inflammation	Not Applicable	NCT01127113	Suspended
PET/MRI	^{64}Cu-NOTA-PSMAi-PEG-Cy5.5-C' dots	Prostate Cancer	Phase 1	NCT04167969	Recruiting
PET	^{89}Zr-Df-CriPec® Docetaxel	Solid Tumor	Phase 1	NCT03712423	Recruiting
PET	^{89}Zr-DFO-cRGDY-PEG-Cy5-C' dots	Brain Cancer	Phase 1	NCT03465618	Recruiting
PET	^{124}I-cRGDY-PEG-dots	Metastatic Melanoma Patients, Malignant Brain Tumors	Not Applicable	NCT01266096	Active, not recruiting
SPECT/CT	^{188}Re-BMEDA-liposome	Tumors	Phase 1	NCT02271516	Unknown
SPECT/CT	^{99m}Tc sulfur colloid	Hepatocellular Carcinoma Intrahepatic Cholangiocarcinoma Liver Cancer Vascular Thrombosis	Not Applicable	NCT02881554	Recruiting
Optical Imaging	fluorescent cRGDY-PEG-Cy5.5-C dots	Head and Neck Melanoma, Breast Cancer, Colorectal Cancer	Phase 1| Phase 2	NCT02106598	Recruiting
Optical Imaging	ONM-100	Breast Cancer, Head, and Neck Squamous Cell Carcinoma, Colorectal Cancer, Prostate Cancer, Ovarian Cancer, Urothelial Carcinoma, Non-small Cell Lung Cancer	Phase 2	NCT03735680	Recruiting